



Mechanistic insights on C–O and C–C bond activation and hydrogen insertion during acetic acid hydrogenation catalyzed by ruthenium clusters in aqueous medium



Junnan Shangguan^a, Mariefel V. Olarte^b, Ya-Huei (Cathy) Chin^{a,*}

^a Department of Chemical Engineering and Applied Chemistry, University of Toronto, Toronto, Canada

^b Institute for Integrated Catalysis, Pacific Northwest National Laboratory, 902 Battelle Boulevard, Richland, WA 99352, USA

ARTICLE INFO

Article history:

Received 11 January 2016

Revised 29 April 2016

Accepted 30 April 2016

Keywords:

Carboxylic acid
Hydrogenation
Ruthenium
Proton transfer
Aqueous phase catalysis
C–O bond activation
Hydrogen insertion
Reduction mechanism
Water solvation

ABSTRACT

Catalytic pathways for acetic acid (CH₃COOH) and hydrogen (H₂) reactions on dispersed Ru clusters in the aqueous medium and the associated kinetic requirements for C–O and C–C bond cleavages and hydrogen insertions are established from rate and isotopic assessments. CH₃COOH reacts with H₂ in steps that either retain its carbon backbone and lead to ethanol, ethyl acetate, and ethane (47–95%, 1–23%, and 2–17% carbon selectivities, respectively) or break its C–C bond and form methane (1–43% carbon selectivities) at moderate temperatures (413–523 K) and H₂ pressures (10–60 bar, 298 K). Initial CH₃COOH activation is the kinetically-relevant step, during which CH₃C(O)–OH bond cleaves on a metal site pair at Ru cluster surfaces nearly saturated with adsorbed hydroxyl (OH*) and acetate (CH₃COO*) intermediates, forming an adsorbed acetyl (CH₃CO*) and hydroxyl (OH*) species. Acetic acid turnover rates increase proportionally with both H₂ (10–60 bar) and CH₃COOH concentrations at low CH₃COOH concentrations (<0.83 M), but decrease from first to zero order as the CH₃COOH concentration and the CH₃COO* coverages increase and the vacant Ru sites concomitantly decrease. Beyond the initial CH₃C(O)–OH bond activation, sequential H-insertions on the surface acetyl species (CH₃CO*) lead to C₂ products and their derivative (ethanol, ethane, and ethyl acetate) while the competitive C–C bond cleavage of CH₃CO* causes the eventual methane formation. The instantaneous carbon selectivities toward C₂ species (ethanol, ethane, and ethyl acetate) increase linearly with the concentration of proton-type H^{δ+} (derived from carboxylic acid dissociation) and chemisorbed H*. The selectivities toward C₂ products decrease with increasing temperature, because of higher observed barriers for C–C bond cleavage than H-insertion. This study offers an interpretation of mechanism and energetics and provides kinetic evidence of carboxylic acid assisted proton-type hydrogen (H^{δ+}) shuffling during H-insertion steps in the aqueous phase, unlike those in the vapor phase, during the hydrogenation of acetic acid on Ru clusters.

© 2016 Elsevier Inc. All rights reserved.

1. Introduction

Environmental and economic impacts have driven the bio-economy, which utilizes lignocellulosic biomass as a precursor instead of the conventional fossil based feedstock for fuel and chemical synthesis. Fast pyrolysis is a thermal chemical conversion route that transforms biomass to bio-oil, useful as a sustainable liquid energy carrier [1,2]. The bio-oil contains oxygenates with diverse functional groups (i.e., phenolic, carboxylic, furanic, carbonyl, alcohol functions), along with a large fraction of water [1,3]. Its high oxygen content lowers the heating value and thermal stability against polymerization and decomposition, thus making it

unsuitable to be used directly as a liquid fuel. Hydrotreating of bio-oil at high temperatures (673–778 K) and H₂ pressures (80–135 bar) removes the various functional groups, thus increasing the effective hydrogen-to-carbon ratios and heating values [4]. Hydrodeoxygenation of bio-oil at moderate temperatures (<673 K) and hydrogen pressures (<100 bar) remains as an attractive route, because such conditions minimize the cracking reactions of small oxygenates (e.g., acetic acid). Lower temperatures also prevent undesirable polymerization, which causes carbon losses from the liquid stream, catalyst deactivation, and undesirable operational shutdowns [5].

Catalytic hydrogenation of phenolic compounds [6–9], furanic compounds [10–12], and carboxylic acids [13–18] in aqueous media has remained as the subject of active research, as it is a critical step in bio-oil refining. Hydrogenation of carboxylic acids,

* Corresponding author.

E-mail address: cathy.chin@utoronto.ca (Ya-Huei (Cathy) Chin).

which transforms the acids to alcohols, is a crucial step to reduce the acid functionality and thus improve the stability of bio-oils. The rates of carboxylic acid hydrogenation [15,18] are at least an order of magnitude lower than those of carbonyl [19,20], phenolic [6,7,21], and furanic [10–12,20] compounds in the aqueous phase (e.g., turnover rates of $2.1 \times 10^1 \text{ h}^{-1}$ for acetic acid on Ru/C [18] vs. $2.1 \times 10^3 \text{ h}^{-1}$ for acetaldehyde on Ru/Al₂O₃ [20] at 373 K, turnover rates of 1.0 h^{-1} for acetic acid [18] vs. $4.2 \times 10^3 \text{ h}^{-1}$ for phenol [21] on Pd/C at 473 K). Hydrogenation of acetic acid, the simplest carboxylic acid, over supported transition metals or metal oxides produces acetaldehyde and ethanol (Pt/TiO₂ [22], Fe/SiO₂ [23], Fe/C [23], Cr₂O₃ [24], and Fe₂O₃ [23–25]), methane and carbon oxides (CO and CO₂) (Pt/SiO₂ [26,27]), and acetone (Fe/C [23], ZrO₂ [24], CeO₂ [24], ZnO [24], and MnO [24]) in the vapor phase. This reaction, when carrying out in the aqueous phase, requires catalysts that are stable at high temperatures and in acidic solution. Transition metals (Raney Ni [18], Raney Cu [18], Ru/C [16,18], Ru/ZrO₂ [15], Ru/Al₂O₃ [15], Pd/C [18], Pt/C [13,18], and Pt/TiO₂ [13]) are active catalysts for hydrogenation reactions in the aqueous phase, especially dispersed Ru clusters, which selectively convert acetic acid to ethanol with carbon selectivities as high as 70% (at 373–573 K, 10–50 bar H₂, with methane, ethane, and ethyl acetate as the side products) [13–18]. The reaction pathways and their detailed mechanism leading to the formation of ethanol and the various side products have not yet been unequivocally established. Density Functional Theory (DFT) was used to elucidate the activation and hydrogenation of acetic acid on Group VIII metal surfaces {Pt(111) [18,28], Pd(111) [18,29–31], Ru(0001) [16,18,32]}, but these theoretical calculations were developed for vapor phase reactions and surfaces free of reactive intermediates, and thus cannot be directly applied to describe the reaction energetics for acetic acid hydrogenation in the aqueous medium. Metal surfaces during the aqueous phase reactions are predominantly covered with hydroxyl species and activation enthalpies and entropies are influenced largely by water solvation and hydrogen bonds. Specifically, a rigorous, quantitative explanation on the relative site-time-yields for ethanol and methane, the extents of several side reactions, the coverages and catalytic roles of surface intermediates, the specific role of H₂O molecules (solvent), and their temperature dependence have remained elusive.

Here, we report the catalytic pathways and the associated kinetics during acetic acid hydrogenation (CH₃COOH–H₂) in the aqueous phase that lead to the formation of ethanol, other C₂ side products such as ethyl acetate and ethane, and methane at moderate temperatures (413–523 K) and hydrogen pressures (10–60 bar H₂, measured at 298 K). We propose a closed sequence of elementary steps, which encompasses the initial CH₃C(O)–OH cleavage, followed by sequential H-insertion reactions with either H adatom (H*) or proton (H⁺), the latter is afforded by the additional catalytic role of CH₃COOH as a proton-shuffling catalyst, or by the competing C–C bond cleavage step on Ru cluster surfaces covered predominantly with hydroxyl species. We interpret the observed activation barrier required for CH₃COOH activation into energetic contributions from the kinetically-relevant step and heats of adsorption of the reactive intermediates, and gas phase bond dissociation energies (BDE), considering the H₂O solvation effects and the predominant site occupation by OH* species. We find that increasing the reaction temperature largely promotes the undesirable C–C bond cleavage step that leads to methane, because of its higher observed barrier than those of H-insertions. This work offers mechanistic insights for the hydrogenation of carboxylic acid (CH₃COOH) and demonstrates a specific route for carboxylic acid facilitated proton (H⁺) addition onto the surface acetyl species on dispersed Ru clusters in the aqueous medium.

2. Experimental methods

2.1. Synthesis and characterizations of Ru clusters supported on activated carbon powders

Activated carbon powders [Norit, Activated Carbon, SX ULTRA CAT 8020-1, 1200 m² g⁻¹, 90% of the particles (*D*₉₀) are <100 μm, pore volume of 1.4 cm³ g⁻¹] were loaded into a quartz boat, placed in a muffler furnace, and then treated under flowing He (Linde certified standard, 99.999%, 0.60 cm³ g⁻¹ s⁻¹) by increasing the temperature at 0.03 K s⁻¹ to 573 K, holding for 7 h, and then cooled to 298 K before Ru incorporation (4 wt.%) by incipient wetness impregnation method. The incipient wetness impregnation was carried out via two consecutive impregnation steps. Within each step, an aqueous Ru precursor, prepared from mixing Ru(NO)(NO₃)₃ (Sigma Aldrich, 1.2 wt.% Ru, CAS Number: 34513-98-9) with doubly-deionized water (>18 MΩ cm), was added dropwise to the carbon powder. After each impregnation step, the sample was placed in the ambient environment for 12 h before further heating from ambient environment to 348 K and keeping at 348 K for another 12 h. The fully-impregnated sample was treated under flowing 5% H₂/He (Linde certified standard, 0.27 cm³ g⁻¹ s⁻¹) by heating at 0.16 K s⁻¹ to 723 K for 5 h. The sample was then cooled to ambient temperature (~0.08 K s⁻¹) under flowing of 5% H₂/He (Linde certified standard, 0.27 cm³ g⁻¹ s⁻¹) while purging with He (Linde certified standard, 99.999%, 0.10 cm³ g⁻¹ s⁻¹) for 1 h, before exposure to flowing 5.5% O₂ (Linde certified standard, 0.15 cm³ g⁻¹ s⁻¹) at 298 K for 1 h. The sample was then exposed to ambient air.

The mean Ru cluster diameter was determined from the amount of irreversibly adsorbed H₂, measured with a volumetric adsorption-desorption apparatus over 0–13 kPa H₂ at an incremental pressure of ~495 Pa at 313 K. The catalyst was treated *in-situ* in flowing H₂ (Linde, 99.99%, 0.8 cm³ g⁻¹ s⁻¹), by heating from ambient temperature to 723 K at 0.03 K s⁻¹ and holding isothermally at 723 K for 1 h before exposing to dynamic vacuum (<5 × 10⁻² Pa) at 723 K for at least 12 h and then cooling to 313 K for the H₂ uptake measurements. Two sets of H₂ uptakes were measured, and between them, the catalyst was evacuated under dynamic vacuum (1 × 10⁻⁶ Pa to 5 × 10⁻² Pa) for 5 min at 313 K. The amount of irreversibly adsorbed H₂ was determined by the difference between the H₂ uptakes obtained from extrapolating the two isotherms to zero pressures. Mean cluster diameter (*d*_{avg}) was obtained by assuming an atomic ratio for chemisorbed H-to-surface Ru of unity and calculated based on the following equation [33]:

$$d_{\text{avg}} = \frac{6v_m}{Da_m} \quad (1)$$

where *v*_m (13.65 × 10⁻³ nm³ [28,33]) is the average volume occupied by a single Ru-atom in the bulk phase, *a*_m (9.9 × 10⁻² nm² [28]) is the average surface area occupied by an exposed Ru surface atom, and *D* is the dispersion (atomic ratio of surface to bulk Ru). The number 6 in the equation comes from the hemispherical cluster assumption. The dispersion value was 7.0% and the mean cluster diameter was 13 nm.

2.2. Rate and selectivity assessments with an isothermal, ideal batch stirred tank reactor

Rates and selectivities for CH₃COOH–H₂ reactions in the aqueous phase were measured with an isothermal batch stirred tank reactor equipped with a mechanical stirrer (300 cm³, Parr Instrument 4560 Mini Bench Top Reactors, Hastelloy). Acetic acid aqueous solution [0.00–3.33 M (mol dm⁻³), 100 cm³ mixture of acetic

Table 1

Effects of agitation speed on the initial acetic acid turnover rates during acetic acid and hydrogen reactions on 4.0 wt.% Ru/C catalysts at 473 K in the aqueous phase.

Run #	Stirring speed (rpm)	$TOR_{CH_3COOH}^a$ [$\text{mol} \cdot (\text{mol}_{\text{Ru,surf}} \text{h})^{-1}$]
1	800	1687
2	1350	1617

^a TOR_{CH_3COOH} denotes turnover rate of CH_3COOH per exposed Ru atom, subscript Ru_{surf} denotes a surface Ru atom; 100 cm^3 0.83 M CH_3COOH (aq), 50 bar H_2 , 4.0 wt.% Ru/C (13 nm mean Ru cluster diameter).

acid (Caledon, 99.7%) and doubly-deionized water, >18 M Ω cm) and catalyst powders (4 wt.% Ru/C, 10–300 mg) were added into the autoclave reactor. After purging the reactor with H_2 at the ambient temperature for 5 min, a gas phase internal standard (i.e., propane, Linde, 99.0%, 0.7 bar at 298 K) and H_2 (Linde, 99.99%, 10–60 bar H_2 at 298 K) were introduced to the reactor. The reactor was sealed and then heated to 323 K, at which the agitation speed was set at 600 rpm for 25 min. This step leads to the reduction of Ru clusters without any detectable acetic acid conversion (<0.05%). The stirring was subsequently halted before heating the reactor to the desired reaction temperature (413–543 K), at which the agitation speed was set to 800 rpm and the reaction time was set to zero. Acetic acid conversions were varied (from 0% to 40%) by increasing the reaction time (30–1600 min) but, for the measurements of initial rate and selectivities, their values were kept below 10%. At specific reaction time, the reactor was quenched from the reaction temperature to room temperature within 5 min by immersing the reactor into an ice-water bath. Gas samples were collected using a customized gas sampling system, whereas a small amount of liquid sample (<2 cm^3) was withdrawn from the reactor. The liquid sample was filtrated with a syringe equipped with syringe filter (VWR, 25 mm syringe filter, 0.2 μm polypropylene membrane). Internal standards [i.e., ~0.02 cm^3 1-propanol (Sigma Aldrich, 99.5%) and ~0.15 cm^3 propionic acid (Sigma Aldrich, 99.5%)] were added to the liquid sample (0.5–1.5 cm^3) before its quantification in order to obtain the overall carbon balance. All the liquid and gas products were collected and quantified with a gas chromatograph (Agilent 7890A) equipped with a DB-1 column (30 m \times 320 μm \times 1 μm), which was connected to a flame ionization detector (FID) for quantifications of hydrocarbons and oxygenates, and a Supel-Q column (30 m \times 530 μm \times 1 μm), which was connected to a thermal conductivity detector (TCD) for CO and CO_2 quantifications.

Measurements of time-dependent concentration profiles were carried out with 1.67 M acetic acid aqueous solution and 50 bar of H_2 at 298 K. The start-up procedure for this reaction was described above, but the reactor was quenched periodically (every 30–300 min) at periods depending on the rate of change in acetic acid concentrations, followed by samplings of the gas and liquid phases with the method described above. After sampling, the reactor was purged with H_2 for 5 min, followed by introducing propane (the internal standard for the gas phase quantification, 0.7 bar at 298 K) and 50 bar of H_2 at 298 K. The reactor was then brought

to the reaction temperature (473 K) to re-initiate the reaction. The reaction time is defined as the duration at which the reactor remained at the reaction temperature and under a constant agitation speed of 800 rpm. This does not include the duration of gas and liquid phase samplings at room temperature as well as that during re-introduction of H_2 and propane into the reactor.

The extent of H_2 – D_2O isotopic scrambling was probed with H_2 – D_2O reactions on 20 mg of 4 wt.% Ru/C at 373 K. The reactor was first filled with 49 g D_2O , purged with H_2 , and then charged with 50 bar H_2 at standard conditions. The reactor was then brought to 373 K and the agitation speed was set to 800 rpm for 30 min. After the reaction, the gas was released, and H_2O , HDO, and D_2O in the liquid phase were quantified with a mass spectrometer (Model 5975C, Agilent).

3. Results and discussion

3.1. Elimination of external and internal mass transport limitations in rate assessments

Acetic acid and hydrogen reactions in the aqueous medium involve transports of H_2 (g) and acetic acid from the fluid phase to the surfaces of Ru clusters, which are dispersed inside the pores of activated carbon supports. We first probe and confirm the complete removal of both external and internal mass transport limitations in the batch reactor, when operating under the conditions reported herein. Table 1 compares the initial turnover rates of acetic acid (TOR_{CH_3COOH} , per exposed Ru atom) for acetic acid and hydrogen reactions [0.83 M CH_3COOH and 50 bar H_2] on dispersed Ru clusters [4.0 wt.% Ru/C, 13 nm mean Ru cluster diameter (d_{avg}), 90% of the carbon particle diameters (D_{90}) is <100 μm] at 473 K for two agitation speeds of 800 and 1350 rpm. The turnover rates remained unaffected by the extent of agitation within the experimental errors ($\pm 10\%$ for turnover rates). These agitation speeds were previously used in similar reactor configurations (Parr, Series 4843, 300 cm^3) to assess the kinetics for phenol hydrogenation {473 K, 700 rpm, 40 bar H_2 , 56,000 $\text{mol} \cdot (\text{mol}_{\text{Ni,surf}} \text{h})^{-1}$ (subscript Ni_{surf} denotes Ni surface atom), Ni/H-ZSM-5 [7]} and 2-butanone hydrogenation {313 K, 900 rpm, 14 bar H_2 , >4800 $\text{mol} \cdot (\text{mol}_{\text{Ru,surf}} \text{h})^{-1}$ (subscript Ru_{surf} denotes Ru surface atom), Ru/C [34]}, both of which occur at rates higher than the highest turnover rates reported here [4200 $\text{mol} \cdot (\text{mol}_{\text{Ru,surf}} \text{h})^{-1}$ (subscript Ru_{surf} denotes Ru surface atom)], and have been shown to be free of external transport limitations. These previous studies and conclusions, taken together with the results shown in Table 1, have allowed us to rule out any influence of external transport on the rate and selectivity data measured herein.

Weisz–Prater criterion was used to probe the potential internal transport restrictions (within the carbon particles). The dimensionless Weisz–Prater parameter (ϕ_{WP}) [35] represents the ratio of reaction to diffusion rates inside the catalyst pores:

$$\phi_{\text{WP},i} = \frac{r_i R_p^2}{[i] D_{\text{eff},i}} \quad (2)$$

Table 2

Estimated Weisz–Prater parameters (ϕ_{WP}) for acetic acid and hydrogen reactions on 4 wt.% Ru/C catalysts at 523 K.^a

Reactant i	r_i ($\text{mol cm}^{-3} \text{s}^{-1}$) ^b	R_p (cm)	$C_{S,A}$ (mol cm^{-3}) ^c	D_{eff} ($\text{cm}^2 \text{s}^{-1}$)	ϕ_{WP}
CH_3COOH	9.0×10^{-6}	1.0×10^{-2}	1.7×10^{-3}	2.5×10^{-4}	2.1×10^{-3}
H_2	1.8×10^{-5}	1.0×10^{-2}	2.8×10^{-5}	6.0×10^{-4}	1.0×10^{-1}

^a 1.67 M CH_3COOH (aq), 50 bar H_2 ; 4 wt.% Ru/C (13 nm mean Ru cluster diameter). r_i ($\text{mol cm}^{-3} \text{s}^{-1}$, where $i = CH_3COOH, H_2$) is the observed reaction rate per catalyst volume; R_p (cm) is the average radius of carbon support; $D_{\text{eff},i}$ ($\text{cm}^2 \text{s}^{-1}$) is the effective diffusivity of reactant i ($i = CH_3COOH, H_2$); ϕ_{WP} is the Weisz–Prater parameters [35].

^b Based on $CH_3COOH + 2H_2 \rightarrow CH_3CH_2OH + H_2O$, $r_{H_2} = 2r_{CH_3COOH}$.

^c C_{S,H_2} was calculated using Henry's Law constant ($K_{H_2} = 2.9 \times 10^6$) obtained from temperature and pressure dependence of H_2 solubility in water (297–616 K, 0–48 bar) [43].

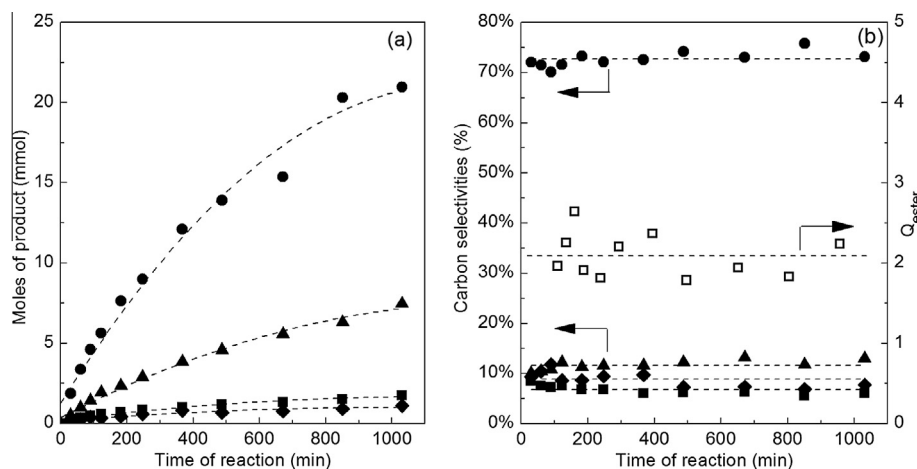
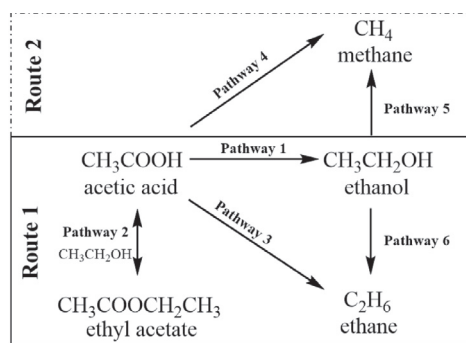


Fig. 1. (a and b) Time-dependent (a) product evolution profiles of ethanol (●), methane (▲), ethane (■), and ethyl acetate (◆), (b) carbon selectivities of ethanol (●), methane (▲), ethane (■), and ethyl acetate (◆) and esterification reaction quotient (\square) for esterification reaction of acetic acid with ethanol ($Q_{\text{ester}} = [\text{CH}_3\text{COOCH}_2\text{CH}_3][\text{H}_2\text{O}] / \{[\text{CH}_3\text{COOH}][\text{CH}_3\text{CH}_2\text{OH}]\}^{-1}$, Eq. (3b)) during $\text{CH}_3\text{COOH}-\text{H}_2$ reactions on dispersed Ru clusters [1.67 M CH_3COOH (aq), 100 cm^3 aqueous solution, 100 mg 4 wt.% Ru/C (13 nm mean Ru cluster diameter), 473 K, 50 bar H_2].

where r_i ($\text{mol cm}^{-3} \text{s}^{-1}$, where $i = \text{CH}_3\text{COOH}, \text{H}_2$) is the observed reaction rate per catalyst volume, R_p (cm) is the average radius of catalyst particles, $[i]$ (mol cm^{-3} , where $i = \text{CH}_3\text{COOH}, \text{H}_2$) is the concentration of reactant at the catalyst surfaces, and $D_{\text{eff},i}$ ($\text{cm}^2 \text{s}^{-1}$) is the effective diffusivity of reactant i ($i = \text{CH}_3\text{COOH}, \text{H}_2$). The Weisz–Prater parameters for acetic acid and hydrogen ($\phi_{\text{WP},i}$, $i = \text{CH}_3\text{COOH}, \text{H}_2$) were determined for the highest turnover rates measured in our study [$r_{\text{CH}_3\text{COOH}} = 4200 \text{ mol} \cdot (\text{mol}_{\text{Ru,surf}} \text{h})^{-1}$ using the effective diffusivities (D_{eff}) of CH_3COOH in H_2O and of H_2 in the $\text{CH}_3\text{COOH}-\text{H}_2\text{O}$ mixture], determined from empirical equations taken from the literature ($D_{\text{eff},\text{CH}_3\text{COOH}} = 2.5 \times 10^{-4} \text{ cm}^2 \text{ s}^{-1}$, $D_{\text{eff},\text{H}_2} = 6.0 \times 10^{-4} \text{ cm}^2 \text{ s}^{-1}$ at 523 K) [36–38]. These calculations led to estimated $\phi_{\text{WP},\text{CH}_3\text{COOH}}$ and $\phi_{\text{WP},\text{H}_2}$ values of 2.1×10^{-3} and 1.0×10^{-1} , respectively, as summarized in Table 2. These values are at least a third of the critical values required for the effectiveness factor (η) to decrease below 0.95, previously determined to be 0.6 for first order and 0.3 for second order reactions [39]. These Weisz–Prater parameters much smaller than the critical values that cause internal transport restrictions and the rate data independent of agitation speed (for speeds exceeding 800 rpm) led us to conclude that rate data measured with the current reactor configurations at an agitation speed above 800 rpm reflect intrinsic catalytic events at Ru cluster surfaces, uncorrupted by inter-phase and intra-particle mass transport limitations.

3.2. Catalytic pathways for acetic acid and hydrogen reactions on Ru clusters in the aqueous phase

Fig. 1 shows the evolution of carbon products (ethanol, ethyl acetate, ethane, and methane, Fig. 1a) and carbon selectivities (Fig. 1b) during aqueous phase acetic acid and hydrogen reactions as a function of reaction time (30–1031 min, 100 cm^3 , 1.67 M acetic acid in H_2O , 50 bar H_2) on 4.0 wt.% Ru/C catalyst (13 nm mean Ru cluster diameter) at 473 K in a gradientless batch reactor (see Section 3.1 for the assessments and removal of transport limitations). Acetic acid and hydrogen reactions proceed via four different pathways, as summarized in Scheme 1. These pathways are as follows: direct hydrogenation to ethanol (Pathway 1), esterification of acetic acid with ethanol to ethyl acetate (Pathway 2), hydrogen-insertion and oxygen removal to ethane (Pathway 3), and carbon–carbon bond cleavage and hydrogenation to methane (Pathway 4). Carbon oxides (CO and CO_2) were not detected at



- Pathway 1:** direct hydrogenation to ethanol;
- Pathway 2:** esterification of acetic acid with ethanol to ethyl acetate;
- Pathway 3:** hydrogen-insertion and oxygen removal to ethane;
- Pathway 4:** carbon–carbon bond cleavage and hydrogenation to methane;
- Pathway 5:** ethanol decomposition to methane;
- Pathway 6:** ethanol decomposition to ethane.

(\rightarrow) denotes an irreversible pathway and \leftrightarrow denotes a quasi-equilibrated pathway)

Scheme 1. Catalytic pathways for $\text{CH}_3\text{COOH}-\text{H}_2$ reactions on Ru clusters in the aqueous phase.

any reaction time (<0.1% of carbon selectivities), consistent with the absence of CO and CO_2 formation from acetic acid– H_2 reaction on Ru/C under similar reaction conditions (14 nm mean Ru cluster diameter supported on carbon, 373–498 K, 50 bar [18]). The carbon selectivities (Fig. 1b) remain insensitive to reaction time for the entire reaction period (30–1031 min). The initial carbon selectivity values of 72.1%, 9.3%, 8.5%, and 10.1% toward ethanol, ethyl acetate, ethane, and methane, respectively, at 473 K and 50 bar H_2 , are consistent with those reported previously on Ru catalysts under similar conditions (74.0%, 10.3%, 1.6%, and 14.0%, respectively, on 14 nm mean Ru cluster diameter supported on carbon, 458 K, at 50 bar H_2 (at 458 K) [18]).

The reversibility of Pathway 1 and Pathway 2 and their contributions to methane and ethane formation were probed with reactions of either ethanol with hydrogen (Entries 3 and 4, Table 3) or ethyl acetate with hydrogen (Entries 6 and 7, Table 3) at similar reaction conditions (473 K, 50 bar H_2 , 0.22 M $\text{CH}_3\text{CH}_2\text{OH}$ or 0.11–1.1 M $\text{CH}_3\text{COOCH}_2\text{CH}_3$, 100 cm^3 aqueous solution); their carbon selectivities and forward turnover rates (per exposed Ru atom)

Table 3

Summary of conversions, turnover rates (TOR), and carbon selectivities for aqueous phase acetic acid, ethanol, acetaldehyde, ethyl acetate reactions with hydrogen at 473 K^a and D₂O–H₂ isotopic scrambling results at 373 K^b.

Entry	Reactant mixture	Reactant (wt.%)	Catalyst (mg)	Time (min)	Conversion (%)	TOR ^c × 10 ³	Carbon selectivities (%)				
							CH ₄	C ₂ H ₆	C ₂ H ₅ OH	CH ₃ COOH	
1	CH ₃ COOH–H ₂ –H ₂ O	10	100 ^a	30	01.5	1.89	10.6	08.9	75.6	–	
2	CH ₃ COOH–H ₂ –H ₂ O	10	0 ^a	120	N.D.	N.A.	N.D.	N.D.	N.D.	N.D.	
3	C ₂ H ₅ OH–H ₂ –H ₂ O	1	50 ^a	60	02.5	0.41	92.1	7.9	–	–	
4	C ₂ H ₅ OH–H ₂ –H ₂ O	1	0 ^a	300	N.D.	N.A.	N.D.	N.D.	N.D.	N.D.	
5	CH ₃ CHO–H ₂ –H ₂ O	0.1	20 ^a	60	100	>4.10	5.2	1.0	93.8	N.D.	
6	CH ₃ COOC ₂ H ₅ –H ₂ –H ₂ O	1	0 ^a	300	99.5	N.A.	N.D.	N.D.	45.0	55.0	
7	CH ₃ COOC ₂ H ₅ –H ₂ –H ₂ O	10	50 ^a	126	98.9	>38.6	3.6	0.2	40.4	55.8	
							Isotope distributions (%)				
							D ₂ O	HDO	H ₂ O		
8	D ₂ O–H ₂	100	20 ^b	30	28.0	N.A.	72.0		18.8	9.2	

N.D.: undetectable.

N.A.: unavailable.

^a 50 bar H₂ at 298 K; 4 wt.% Ru/C (13 nm mean Ru cluster diameter).

^b The isotopic exchange data were obtained at 373 K, 50 bar H₂, the conversion were referring to the fraction of D₂O exchanged {conversion = [n(HDO) + n(H₂O)] · [n(HDO) + n(H₂O) + n(D₂O)]⁻¹, where n(i) is the molar of species i, i = D₂O, HDO, or H₂O}.

^c Per Ru surface atom [mol · (mol_{Ru,surf} h)⁻¹].

are summarized in Table 3. Reactions of ethanol and hydrogen without catalysts did not lead to ethanol conversions above detectable limit (<0.01% conversion), even after 6 h (Entry 4, Table 3). Ethanol and hydrogen reactions on 4.0 wt.% Ru/C catalysts (Entry 3, Table 3), however, occur at comparable rates with acetic acid and hydrogen reactions [410 mol_{C₂H₅OH} · (mol_{Ru,surf} h)⁻¹ (Entry 3) vs. 1890 mol_{CH₃COOH} · (mol_{Ru,surf} h)⁻¹ (Entry 1), Table 3]. In fact, the pseudo first-order rate constant ratio for ethanol–hydrogen to acetic acid–hydrogen reactions { $k_{\text{CH}_3\text{CH}_2\text{OH}}(k_{\text{CH}_3\text{COOH}})^{-1}$, where $k_{\text{CH}_3\text{CH}_2\text{OH}} = r_{\text{CH}_3\text{CH}_2\text{OH}}[\text{CH}_3\text{CH}_2\text{OH}]^{-1}$ and $k_{\text{CH}_3\text{COOH}} = r_{\text{CH}_3\text{COOH}}[\text{CH}_3\text{COOH}]^{-1}$ } was 0.87 at 473 K (50 mg Ru catalyst, 50 bar H₂). The reaction (ethanol and hydrogen) led predominantly to methane and a small amount of ethane (92.1% and 7.9% carbon selectivities, respectively, Entry 3, Table 3) without detectable acetic acid formation. These results confirm that acetic acid direct hydrogenation (Pathway 1) is irreversible, but ethanol can decompose in sequential reactions to form methane (Pathway 5) and ethane (Pathway 6). Reactions of ethyl acetate and water in the absence of a catalyst form nearly equimolar acetic acid and ethanol (Entry 6, Table 3) via the reverse esterification reaction in homogeneous phase. The esterification reaction is given by



The reaction quotient for the esterification reaction, Q_{ester} , is

$$Q_{\text{ester}} = \frac{[\text{CH}_3\text{COOCH}_2\text{CH}_3][\text{H}_2\text{O}]}{[\text{CH}_3\text{COOH}][\text{CH}_3\text{CH}_2\text{OH}]} \quad (3b)$$

The reaction quotient Q_{ester} remained essentially unchanged at 2.1 ± 0.3 over the entire reaction period at 473 K, as shown in Fig. 1b, and equaled the expected equilibrium constant (K_{eq}) of 2.3, predicted for this reaction (Eq. (3a)) in the aqueous phase and at this temperature (473 K) [40]. Thus, the relative concentrations of ethyl acetate and ethanol in the product are dictated strictly by thermodynamics.

The overall reaction network, which includes the primary (Pathways 1, 3, 4) and secondary (Pathways 2, 5, 6) reactions, is summarized in Scheme 1. These reaction pathways (Pathways 1–6) are categorized into two routes, depending on whether the carbon backbone of acetic acid was altered. These pathways are as follows: (1) Route 1, direct H-insertion, which leads to the formation of ethanol, ethane, and ethyl acetate, and (2) Route 2, C–C bond cleavage, which leads to the formation of methane. In

what follows, we first interrogate the specific catalytic requirements and kinetic dependencies for the two competing reaction routes (Section 3.3), propose a mechanism consistent with the observed rate dependencies and density functional theory calculations on Ru(0001) [16,18,32], derive rate expressions that capture the individual rate of each pathway (Section 3.4), verify the proposed mechanism with H₂–D₂O isotopic exchange studies (Section 3.4), and then discuss the temperature effects on the relative rates of these individual pathways (Section 3.5).

3.3. Kinetic dependencies of aqueous phase CH₃COOH and H₂ reactions on dispersed Ru clusters

Turnover rates for acetic acid conversion (per exposed Ru atom) are denoted as r_{overall} and the site-time-yields for individual species j are denoted as r_j ($j = \text{CH}_3\text{CH}_2\text{OH}$, $\text{CH}_3\text{COOCH}_2\text{CH}_3$, CH_4 , or C_2H_6). $\text{CH}_3\text{CH}_2\text{OH}$, $\text{CH}_3\text{COOCH}_2\text{CH}_3$, and C_2H_6 are formed via Route 1 (Scheme 1), during which H-insertions occur on acetic acid derived intermediates with their C–C backbone intact throughout their catalytic sojourns. The CH_3COOH turnover rates via Route 1 ($\text{CH}_3\text{CH}_2\text{OH}$, $\text{CH}_3\text{COOCH}_2\text{CH}_3$, and C_2H_6) ($r_{\text{Route},1}$) equal the sum of $\text{CH}_3\text{CH}_2\text{OH}$, $\text{CH}_3\text{COOCH}_2\text{CH}_3$, and C_2H_6 site-time-yields ($r_{\text{Route},1} = r_{\text{CH}_3\text{CH}_2\text{OH}} + r_{\text{CH}_3\text{COOCH}_2\text{CH}_3} + r_{\text{C}_2\text{H}_6}$). The rate of ethyl acetate formation was considered here as a single acetic acid turnover, because an acetic acid molecule activates in a kinetically-relevant step that forms an ethanol, which participates in sequential, rapid homogeneous reactions with another acetic acid via the classic Fischer esterification reaction (Eq. (3a)). The reverse esterification reaction (hydrolysis of ethyl acetate) was found to occur spontaneously, even without any catalyst (Section 3.2, Entry 6, Table 3). Each ethyl acetate formation, thus, reflects a catalytic sojourn of an acetic acid molecule in the hydrogenation cycle (Scheme 1). The CH_3COOH turnovers via Route 2 ($r_{\text{Route},2}$) track the rates of C–C bond cleavage in acetic acid, which equal to a half of the methane site-time yields ($r_{\text{Route},2} = 0.5 \times r_{\text{CH}_4}$), as given by the reaction stoichiometry ($\text{CH}_3\text{COOH} + 4\text{H}_2 \rightarrow 2\text{CH}_4 + 2\text{H}_2\text{O}$). Fig. 2 shows the rate dependencies for the overall acetic acid turnovers ($r_{\text{overall}} = r_{\text{Route},1} + r_{\text{Route},2}$) on acetic acid concentration ($[\text{CH}_3\text{COOH}]$, M) and H₂ partial pressure ($[\text{H}_2]$, bar) during CH_3COOH –H₂ reactions in the aqueous phase on dispersed Ru clusters (13 nm mean Ru cluster diameter, 4.0 wt.% Ru/C) at 473 K. The rate dependencies are described by

$$r_{\text{overall}} = k_{\text{eff,overall}} [\text{CH}_3\text{COOH}]^{\alpha_{\text{overall}}} [\text{H}_2]^{\beta_{\text{overall}}} \quad (4)$$

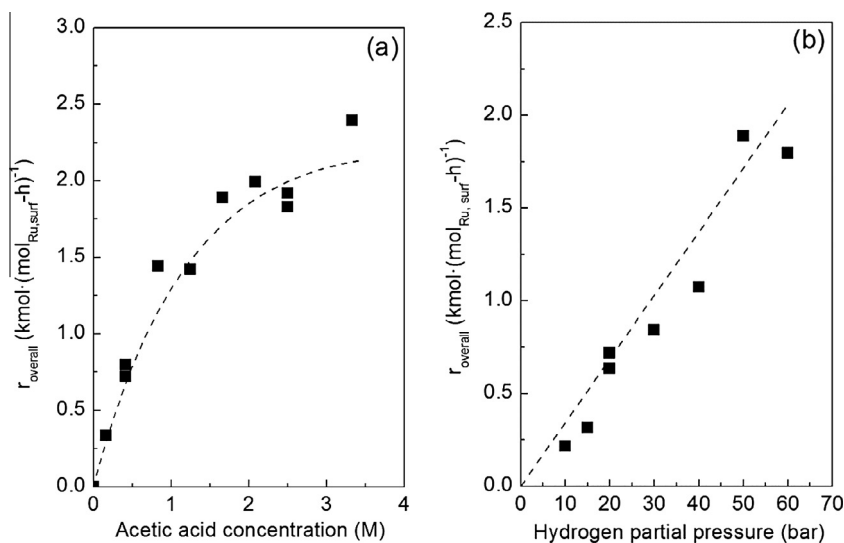


Fig. 2. (a and b) Dependencies of CH_3COOH overall turnover rates (\blacksquare , r_{overall}) on (a) acetic acid concentration (0.00–3.33 M CH_3COOH , 50 bar H_2) and (b) H_2 partial pressure (10–60 bar H_2 , 1.67 M CH_3COOH) at 473 K (100 cm^3 CH_3COOH aqueous solution, 75 mg 4 wt.% Ru/C, 13 nm mean Ru cluster diameter). Dotted lines are the predicted rates from non-linear regression of Eq. (9a).

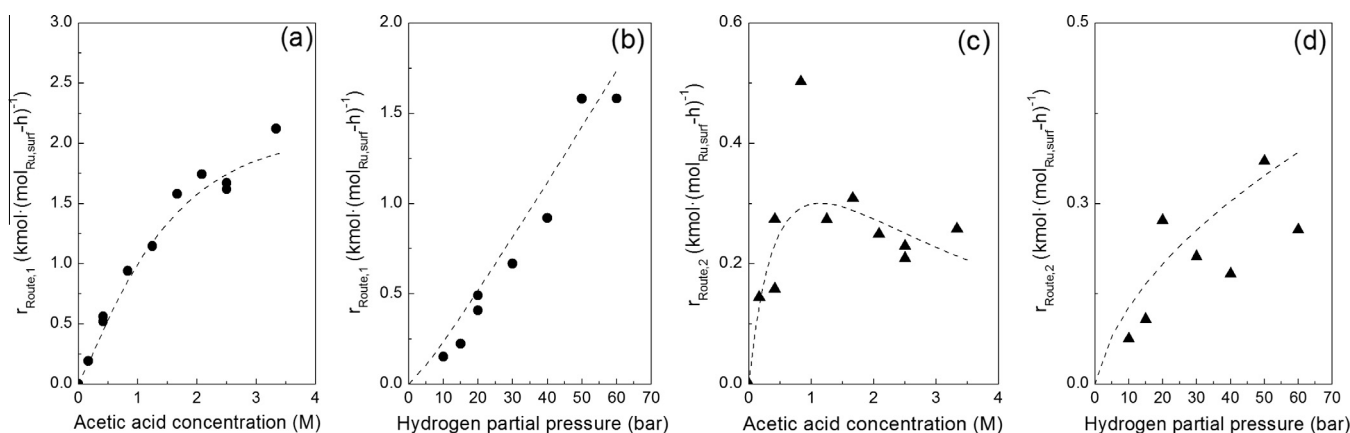


Fig. 3. (a–d) Dependencies of CH_3COOH turnovers via **Route 1** (\bullet , $r_{\text{Route},1}$) on (a) acetic acid concentration (0.00–3.33 M CH_3COOH , 50 bar H_2) and on (b) H_2 partial pressure (10–60 bar H_2 , 1.67 M CH_3COOH); dependencies of CH_3COOH turnovers via **Route 2** (\blacktriangle , $r_{\text{Route},2}$) on (c) acetic acid concentration (0.00–3.33 M CH_3COOH , 50 bar H_2) and on (d) H_2 partial pressure (10–60 bar H_2 , 1.67 M CH_3COOH) at 473 K (100 cm^3 CH_3COOH aqueous solution, 75 mg 4 wt.% Ru/C, 13 nm mean Ru cluster diameter). Dotted lines are the predicted rates from non-linear regression of Eq. (10a).

where $k_{\text{eff,overall}}$ is the effective rate constant; α_{overall} and β_{overall} are the effective reaction orders with respect to CH_3COOH concentration and H_2 partial pressure, respectively. Acetic acid turnover rates (r_{overall}) vary nearly linearly with CH_3COOH ($\alpha_{\text{overall}} = 1.0 \pm 0.1$) for reactions in dilute CH_3COOH solution (0.00–0.83 M), an indication that CH_3COOH activation on Ru surfaces is a kinetically-relevant step. The CH_3COOH dependency, however, becomes less sensitive as the CH_3COOH concentration increases (from 0.83 M to 3.33 M), as CH_3COOH derived intermediates such as surface acetate (CH_3COO^*) and/or adsorbed acetic acid (CH_3COOH^*) occupy a portion of the Ru sites. The turnover rates increase linearly with H_2 pressure ($\beta_{\text{overall}} = 1.1 \pm 0.2$) over the entire H_2 pressure range (10–60 bar). This apparent first order dependence on H_2 may indicate the kinetic relevance of H_2 activation, as reported for benzene hydrogenation on dispersed Ru, Pt, and Pd clusters in organic phases (with cyclohexane, *n*-heptane, or ethyl acetate as the solvent) [41]. We, however, rule out H_2 dissociation as a kinetically-relevant step, because this assumption is inconsistent with the positive dependence of turnover rate on CH_3COOH ($\alpha_{\text{overall}} > 0$) over the entire range and with the much larger rates of hydrogen activation and

hydrogen atom insertion into acetaldehyde, catalyzed by Ru clusters in the aqueous phase under similar conditions [$> 4100 \text{ mol}_{\text{CH}_3\text{CHO}} \cdot (\text{mol}_{\text{Ru,surf}} \text{ h})^{-1}$ ($\text{CH}_3\text{CHO}-\text{H}_2-\text{H}_2\text{O}$, Entry 5) vs. $1890 \text{ mol}_{\text{CH}_3\text{COOH}} \cdot (\text{mol}_{\text{Ru,surf}} \text{ h})^{-1}$ ($\text{CH}_3\text{COOH}-\text{H}_2-\text{H}_2\text{O}$, Entry 1), Table 3].

CH_3COOH turnovers via the specific route (**Route s**, $s = 1$ or 2, as defined in Scheme 1) vary with CH_3COOH and H_2 concentrations according to

$$r_{\text{Route},s} = k_{\text{eff},s} [\text{CH}_3\text{COOH}]^{\alpha_s} [\text{H}_2]^{\beta_s} \quad (5)$$

$k_{\text{eff},s}$ is the effective rate constant for **Route s**; α_s and β_s are the effective reaction orders with respect to CH_3COOH and H_2 for **Route s**, respectively. The rates of CH_3COOH turnovers via **Route 1** ($r_{\text{Route},1} = r_{\text{CH}_3\text{CH}_2\text{OH}} + r_{\text{CH}_3\text{COOCH}_2\text{CH}_3} + r_{\text{C}_2\text{H}_6}$) increase linearly with CH_3COOH at low CH_3COOH concentrations (0.00–0.83 M) and then less than linearly as CH_3COOH increases above 0.83 M, as shown in Fig. 3a. These rates increase more than linearly with H_2 ($\beta_1 = \sim 1.3 \pm 0.1$, Fig. 3b) over the entire H_2 pressure range (10–60 bar). The rates of CH_3COOH turnovers via **Route 2** ($r_{\text{Route},2}$),

Step <i>j</i>	Elementary step <i>j</i>	Equilibrium constant (K_i , $i=\text{CH}_3\text{COOH}$, CH_3COO , H_2 , H_2O , or OH) or rate constant (k_j) for step <i>j</i>
1	$\text{CH}_3\text{COOH}^* \leftrightarrow \text{CH}_3\text{COOH}^*$	$K_{\text{CH}_3\text{COOH}}$
2	$\text{CH}_3\text{COOH}^* \leftrightarrow \text{CH}_3\text{COO}^* + \text{H}^*$	$K_{\text{CH}_3\text{COO}}$
3	$\text{H}_2 + 2^* \leftrightarrow 2\text{H}^*$	K_{H_2}
4	$\text{H}_2\text{O}^* \leftrightarrow \text{H}_2\text{O}^*$	$K_{\text{H}_2\text{O}}$
5	$\text{H}_2\text{O}^* \leftrightarrow \text{H}^* + \text{OH}^*$	K_{OH}
C-OH Cleavage	$\text{CH}_3\text{COOH}^* \rightarrow \text{CH}_3\text{CO}^* + \text{OH}^*$	$k_{\text{C-OH}}$
C-H Insertion	$\text{CH}_3\text{CO}^* + \text{H}^* \rightarrow \text{CH}_3\text{CHO}^* + ^*$	$k_{\text{C-H}}$
O-H Insertion ^a	$\text{CH}_3\text{CO}^* \cdots \text{CH}_3\text{COO}^{\delta-} - \text{H}^{\delta+} + \text{H}^* \rightarrow \text{CH}_3\text{COH}^* \cdots \text{CH}_3\text{COO}^{\delta-} - \text{H}^{\delta+} + ^*$	$k_{\text{O-H}}$
C-C Cleavage	$\text{CH}_3\text{CO}^* + ^* \rightarrow \text{CH}_3^* + \text{CO}^*$	$k_{\text{C-C}}$
6	$\text{CH}_3\text{CHO}^* + \text{H}^* \rightarrow \text{CH}_3\text{CH}_2\text{O}^* + ^*$	$k_{\text{ethoxy formation}}$
7	$\text{CH}_3\text{CHO}^* + \text{H}^* \rightarrow \text{CH}_3\text{CHOH}^* + ^*$	$k_{1\text{-hydroxyethyl formation,1}}$
8	$\text{CH}_3\text{COH}^* + \text{H}^* \rightarrow \text{CH}_3\text{CHOH}^* + ^*$	$k_{1\text{-hydroxyethyl formation,2}}$
9	$\text{CH}_3\text{CH}_2\text{O}^* + \text{H}^* \rightarrow \text{CH}_3\text{CH}_2\text{OH}^* + ^*$	$k_{\text{ethanol formation,1}}$
10	$\text{CH}_3\text{CHOH}^* + \text{H}^* \rightarrow \text{CH}_3\text{CH}_2\text{OH}^* + ^*$	$k_{\text{ethanol formation,2}}$
11 ^b	$\text{CO}^* + \text{H}^* \rightarrow \text{COH}^* + ^*$	k_{11}
12	$\text{COH}^* + \text{H}^* \rightarrow \text{HCOH}^* + ^*$	k_{12}
13	$\text{HCOH}^* + ^* \rightarrow \text{CH}^* + \text{OH}^*$	k_{13}
14	$\text{CH}^* + \text{H}^* \rightarrow \text{CH}_2^* + ^*$	k_{14}
15	$\text{CH}_2^* + \text{H}^* \rightarrow \text{CH}_3^* + ^*$	k_{15}
16	$\text{CH}_3^* + \text{H}^* \rightarrow \text{CH}_4^* + ^*$	k_{16}

(* refers to a Ru surface site, \rightarrow denotes an irreversible step, and \leftrightarrow denotes a quasi-equilibrated step)

^a: $\text{CH}_3\text{COO}^{\delta-} - \text{H}^{\delta+}$ involves as a proton transfer catalyst.

^b: CO methanation in the aqueous phase on Ru surfaces is assumed to proceed from hydroxymethylidyne route described in [48].

Scheme 2. A proposed sequence of elementary steps for CH_3COOH and H_2 reactions in the aqueous phase on Ru clusters. (See above-mentioned reference for further information.)

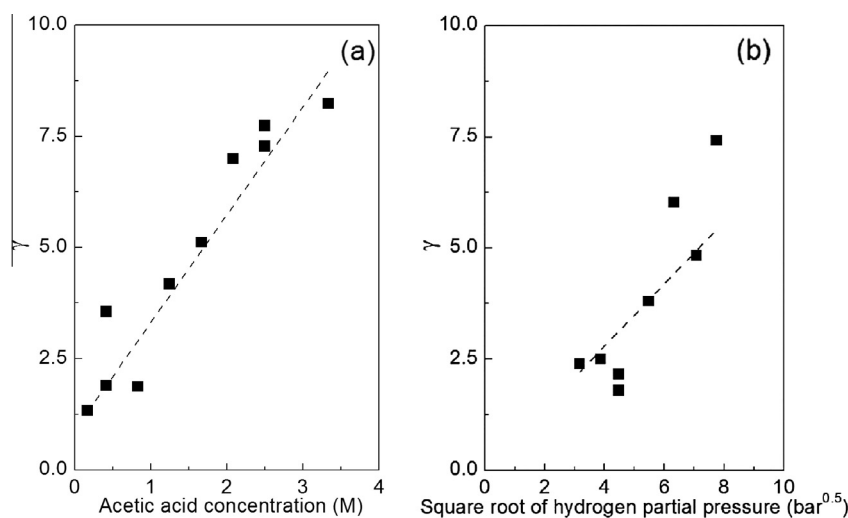


Fig. 4. (a and b) Dependence of instantaneous selectivity ratio γ (■, Eq. (6), Section 3.3) on (a) acetic acid concentration (0.00–3.33 M CH_3COOH , 50 bar H_2) and on (b) square root of hydrogen partial pressure (10–60 bar H_2 , 1.67 M CH_3COOH) at 473 K (100 cm^3 CH_3COOH aqueous solution, 75 mg 4 wt.% Ru/C, 13 nm mean Ru cluster diameter).

which also equal the rates of C–C bond cleavage that lead to methane, first increase with CH_3COOH (from 0.00 M to 0.83 M) and then slowly decrease as the CH_3COOH concentration increases further (in Fig. 3c). These rates increase less than linearly with H_2 pressure ($\beta_2 = \sim 0.6 \pm 0.2$; Fig. 3d). The rate data for **Route 2** (Figs. 3c and 3d) appear to be much noisier than **Route 1**

(Figs. 3a and 3b), because of the much smaller turnover rates for **Route 2** [$63\text{--}321 \text{ mol} \cdot (\text{mol}_{\text{Ru,surf}} \text{h})^{-1}$, $r_{\text{Route,2}}$] compared to those for **Route 1** [$105\text{--}1738 \text{ mol} \cdot (\text{mol}_{\text{Ru,surf}} \text{h})^{-1}$, $r_{\text{Route,1}}$].

The rate ratio of **Route 1** to **Route 2** defines the instantaneous selectivity, γ , which reflects the rate ratio for H-insertion into acetic acid derived intermediates while preserving their C–C bond

($r_{\text{Route},1}$, e.g., $\text{CH}_3\text{CO}^* + \text{H}^* \rightarrow \text{CH}_3\text{CHO}^* + *$, Step C–H Insertion, [Scheme 2](#)) over those for C–C bond cleavage ($r_{\text{Route},2}$, e.g., $\text{CH}_3\text{CO}^* + * \rightarrow \text{CH}_3^* + \text{CO}^*$, Step C–C Cleavage, [Scheme 2](#)):

$$\gamma = \frac{r_{\text{Route},1}}{r_{\text{Route},2}} = \frac{k_{\text{eff},1}}{k_{\text{eff},2}} [\text{CH}_3\text{COOH}]^{(\alpha_1 - \alpha_2)} [\text{H}_2]^{(\beta_1 - \beta_2)} \quad (6)$$

The γ values are shown as a function of CH_3COOH concentration ([Fig. 4a](#), 50 bar H_2) and as a function of the square root of H_2 pressure ($\sqrt{[\text{H}_2]}$, [Fig. 4b](#), 1.67 M CH_3COOH) for 4.0 wt.% Ru/C (13 nm mean Ru cluster diameter) at 473 K. The low CH_3COOH turnover rates via [Route 2](#) [$r_{\text{Route},2}$, 63–213 mol·(mol_{Ru,surf} h)⁻¹, from 10 bar to 60 bar H_2 , [Fig. 3d](#)] cause the apparent larger errors for γ values in [Fig. 4b](#). The γ values are strong functions of and increase with both the CH_3COOH concentration (0.00–3.33 M) and H_2 pressure (10–60 bar) for mechanistic reasons to be discussed later in [Section 3.4](#). These selectivity trends ([Fig. 4](#)) indicate that the rates for the two competing routes ($r_{\text{Route},1}$ and $r_{\text{Route},2}$) vary with CH_3COOH concentration and H_2 pressures differently, because of the differences in their kinetic requirements, specifically the identity of reactive intermediates, their molecularity, and/or the required active sites (and active site ensembles) between these two routes.

3.4. Elementary steps and rate expressions for aqueous phase acetic acid and hydrogen reactions on dispersed Ru clusters

We propose a closed sequence of elementary steps in [Scheme 2](#) that captures the rate dependencies of the overall acetic acid conversion rates and the CH_3COOH turnovers that either retain its C–C backbone ([Route 1](#)) or cleave its C–C bond ([Route 2](#)), consistent with the experimental rate and selectivity data in [Figs. 2–4](#) and [Table 3](#) and the relative energetic trends from Density Functional Theory (DFT) calculations on modeled Ru(0001) single crystal surfaces [[16,18,32](#)].

CH_3COOH first adsorbs on a vacant Ru site (*) (Step 1, [Scheme 2](#)) and forms a chemisorbed CH_3COOH^* species. A portion of CH_3COOH^* cleaves its O–H bond in a step assisted by a vicinal vacant site, which results in a surface acetate (CH_3COO^*) and a chemisorbed hydrogen adatom (H^*) (Step 2). H_2 , the co-reactant, dissolves in the aqueous medium and adsorbs dissociatively on a Ru site pair as two H^* adatoms (Step 3). H_2O as the solvent and an abundant species may adsorb as either H_2O^* or surface hydroxyl (OH^*) and H^* species (Steps 4 and 5, [Scheme 2](#)). These steps (Steps 1–5) occur much more rapidly than the slowest step in the catalytic cycle, the C–O bond activation of $\text{CH}_3\text{C}(\text{O})\text{—OH}^*$ (Step C–OH Cleavage, [Scheme 2](#)), and are therefore considered quasi-equilibrated in the kinetic treatment. $\text{RC}(\text{O})\text{—OH}^*$ ($\text{R} = \text{CH}_3$ or C_2H_5) bond dissociation (Step C–OH Cleavage, [Scheme 2](#)) has been previously proposed from DFT calculations as a kinetically-relevant step on uncovered transition metal surfaces based on either low dissociation barriers (E_a) {50 kJ mol⁻¹ on Ru(0001) [[32](#)], 86 kJ mol⁻¹ on Pd(111) [[29](#)], 80 kJ mol⁻¹ [[27](#)] and 82 kJ mol⁻¹ [[26](#)] on Pt(111)} relative to other steps along the reaction coordinate or low activation free energies to first C–O bond cleavage of CH_3COOH on Rh(111), Pd(111), Ir(111), and Pt(111) along the reaction coordinate [[18](#)]. In contrast to these findings, $\text{CH}_3\text{C}(\text{O})\text{—OH}^*$ dissociation (Step C–OH Cleavage, [Scheme 2](#)) has been previously treated as a quasi-equilibrated step, because of the much higher barrier required for the sequential hydrogenation of ethoxy ($\text{CH}_3\text{CH}_2\text{O}^*$, Step 9) (127 kJ mol⁻¹ for ethoxy hydrogenation vs. 50 kJ mol⁻¹ for $\text{CH}_3\text{C}(\text{O})\text{—OH}$ cleavage) [[16](#)]. The quasi equilibrated C–OH Cleavage step is, however, inconsistent with the rapid CH_3CHO hydrogenation (Entry 5, [Table 3](#), [Section 3.2](#)), occurred only when the sequential H-insertion steps (Steps 6, 7, 9, 10, [Scheme 2](#)) are much faster than the initial CH_3COOH activation

(Step C–OH Cleavage, [Scheme 2](#)). Based on our experimental observations, together with the theoretical calculations [[26,27,29,32](#)], we propose that the initial C–OH bond cleavage (Step C–OH Cleavage) is the kinetically-relevant step during $\text{CH}_3\text{COOH}\text{—H}_2$ reaction on Ru/C in the aqueous phase.

The sequence of elementary steps in [Scheme 2](#), together with pseudo steady-state treatments of the various surface intermediates, which include adsorbed acetic acid (CH_3COOH^*), surface acetyl (CH_3CO^*), chemisorbed hydrogen (H^*), molecularly adsorbed water (H_2O^*), and hydroxyl (OH^*) species, leads to the following rate equation for CH_3COOH turnovers (r_{overall}) (derivation in [Supplementary Information](#), [Section S1](#)):

$$r_{\text{overall}} = \frac{k_{\text{C-OH}} K_{\text{CH}_3\text{COOH}} [\text{CH}_3\text{COOH}]}{(1 + K_{\text{CH}_3\text{COOH}} [\text{CH}_3\text{COOH}] + \frac{K_{\text{CH}_3\text{COOH}} K_{\text{CH}_3\text{COO}} [\text{CH}_3\text{COOH}]}{\sqrt{K_{\text{H}_2} [\text{H}_2]}} + \sqrt{K_{\text{H}_2} [\text{H}_2]} + K_{\text{H}_2\text{O}} [\text{H}_2\text{O}] + \frac{K_{\text{H}_2\text{O}} K_{\text{OH}} [\text{H}_2\text{O}]^2}{\sqrt{K_{\text{H}_2} [\text{H}_2]}})} \quad (7)$$

\uparrow \uparrow \uparrow \uparrow \uparrow \uparrow
 ([*] [CH_3COOH^*] [CH_3COO^*] [H^*] [H_2O^*] [OH^*])

where $k_{\text{C-OH}}$ denotes the elementary rate constant for the activation of $\text{CH}_3\text{C}(\text{O})\text{—OH}$ bond in CH_3COOH (Step C–OH Cleavage, [Scheme 2](#)) and $\theta_{\text{CH}_3\text{COOH}^*}$ and θ_* denote the fractional coverages of CH_3COOH^* and vacant site (*) on Ru cluster surfaces, respectively. Each term in the denominator of [Eq. \(7\)](#) denotes the relative abundances of a type of surface species to the unoccupied Ru sites during steady state catalysis, as noted underneath the equation. The coverages of CH_3COOH^* , CH_3COO^* , H^* , H_2O^* , and OH^* intermediates are given by their respective equilibrium constants ($K_{\text{CH}_3\text{COOH}}$, $K_{\text{CH}_3\text{COO}}$, K_{H_2} , $K_{\text{H}_2\text{O}}$, K_{OH} , as defined in [Scheme 2](#)), CH_3COOH and H_2O concentrations ($[i]$, $i = \text{CH}_3\text{COOH}$, H_2O), and/or H_2 pressure ($[\text{H}_2]$). The coverages of CH_3CO^* , CH_3CHO^* , CH_3COH^* , CH_3CHOH^* , $\text{CH}_3\text{CH}_2\text{O}^*$, and $\text{CH}_3\text{CH}_2\text{OH}^*$ (as appeared in [Scheme 2](#)) are insignificant and therefore omitted from the rate equation, because these intermediates are formed after the kinetically-relevant $\text{CH}_3\text{C}(\text{O})\text{—OH}$ step, later along the reaction coordinate and their reactions with H^* are much faster than the $\text{CH}_3\text{C}(\text{O})\text{—OH}$ dissociation (Entry 5, [Table 3](#), [Section 3.2](#)).

$\text{D}_2\text{O}\text{—H}_2$ reactions ($\text{D}_2\text{O}\text{—to-H}_2$ reactant molar ratio of 4.5:1) on 4.0 wt.% Ru/C gave $\text{D}_2\text{O}\text{—HDO}\text{—H}_2\text{O}$ isotopic distributions of 72.0–18.8–9.2% (Entry 8, [Table 3](#)) within 30 min at 373 K; these distributions are near the expected values at chemical equilibrium (statistical distributions are 67.1–29.6–3.3% $\text{D}_2\text{O}\text{—HDO}\text{—H}_2\text{O}$), even at a much lower temperature than that for acetic acid hydrogenation reaction (373 K vs. 473 K). These results indicate that H_2 and H_2O dissociation (Steps 3–5, [Scheme 2](#)) are equilibrated within the timescale of a CH_3COOH turnover (Step C–OH Cleavage, [Scheme 2](#)). During steady-state reactions in the aqueous phase, Ru cluster surfaces are unlikely to be covered with chemisorbed H^* atoms as the most abundant surface intermediates (MASI), because such surfaces would lead to a reaction order that is either equal to or less than zero for H_2 ($\beta_{\text{overall}} \leq 0$), inconsistent with the purported reaction orders ($\beta_{\text{overall}} = 1.1 \pm 0.2$, [Fig. 2](#), [Section 3.3](#)). The positive H_2 dependence has also been reported for other hydrogenation reactions (0.6 for both levulinic acid (303–343 K) [[42](#)] and 2-butanone (303 K) [[19](#)] hydrogenation) on Ru in the aqueous phase, an indication that the coverages of H^* on Ru cluster surfaces must remain low and insignificant.

The coverage ratios of $\text{OH}^*\text{—to-}^*$ [$\theta_{\text{OH}^*}(\theta_*)^{-1}$], $\text{OH}^*\text{—to-}\text{H}^*$ [$\theta_{\text{OH}^*}(\theta_{\text{H}^*})^{-1}$], and $\text{OH}^*\text{—to-}\text{H}_2\text{O}^*$ [$\theta_{\text{OH}^*}(\theta_{\text{H}_2\text{O}^*})^{-1}$] may be derived from the denominator terms in [Eq. \(7\)](#); their values are dictated by the equilibrium constants K_{H_2} , $K_{\text{H}_2\text{O}}$, and K_{OH} (Steps 3–5, [Scheme 2](#)), H_2O concentration, and H_2 pressure:

$$\frac{\theta_{\text{OH}^*}}{\theta_*} = \frac{K_{\text{H}_2\text{O}} K_{\text{OH}} [\text{H}_2\text{O}]}{\sqrt{K_{\text{H}_2} [\text{H}_2]}} \quad (8a)$$

$$\frac{\theta_{\text{OH}^*}}{\theta_{\text{H}^*}} = \frac{K_{\text{H}_2\text{O}}K_{\text{OH}}}{K_{\text{H}_2}} \frac{[\text{H}_2\text{O}]}{[\text{H}_2]} \quad (8b)$$

$$\frac{\theta_{\text{OH}^*}}{\theta_{\text{H}_2\text{O}^*}} = \frac{K_{\text{OH}}}{\sqrt{K_{\text{H}_2}}[\text{H}_2]} \quad (8c)$$

The equilibrium constants (K_{H_2} , $K_{\text{H}_2\text{O}}$, K_{OH}) are previously determined to be 4.84×10^6 , 2.03, and 4.05×10^5 on Ru(0001) surfaces at 473 K, respectively, without the effects of solvent or other adsorbates by using energies derived from DFT, the Eyring equation, and partition functions [32]. These values and the high concentration of H_2O (52.7 M at 0.83 M CH_3COOH) and H_2 (50 bar in the gas phase, which corresponds to <0.005 M in the aqueous phase at 473 K [43]) give the coverage ratio for OH^* -to- $*$ [$\theta_{\text{OH}^*}(\theta_*)^{-1}$] larger than 2.78×10^5 , OH^* -to- H^* [$\theta_{\text{OH}^*}(\theta_{\text{H}^*})^{-1}$] larger than 1.79×10^3 , and OH^* -to- H_2O^* [$\theta_{\text{OH}^*}(\theta_{\text{H}_2\text{O}^*})^{-1}$] larger than 2.60×10^3 . This translates to a much larger OH^* than $*$, H^* , and H_2O^* coverages ($\theta_{\text{OH}^*} \gg \theta_*$, $\theta_{\text{OH}^*} \gg \theta_{\text{H}^*}$, and $\theta_{\text{OH}^*} \gg \theta_{\text{H}_2\text{O}^*}$, respectively) during steady-state reactions for the rate data in Figs. 2 and 3. The OH^* coverages are expected to be even larger, since OH^* and H_2O^* form thermodynamically more favorable $\text{OH}-\text{H}_2\text{O}$ bilayer structures than the adsorbed H_2O^* bilayer on Ru cluster surfaces in aqueous media [44,45].

CH_3COOH prefers to dissociate and then adsorb as surface acetate (CH_3COO^*) on uncovered Ru(0001) surfaces below 500 K (Steps 1–2, Scheme 2). This was detected by Reflection–Absorption Infrared Spectroscopy (RAIRS) [46] and confirmed from the low barriers required for $\text{RC}(\text{O})\text{O}-\text{H}$ ($\text{R} = \text{CH}_3$, C_2H_5) dissociation {35 kJ mol^{-1} for CH_3COOH [16] and 20 kJ mol^{-1} for $\text{CH}_3\text{CH}_2\text{COOH}$ [32] on Ru(0001)} and higher heats of CH_3COO^* ($Q_{\text{CH}_3\text{COO}^*}$) than CH_3COOH^* adsorption ($Q_{\text{CH}_3\text{COOH}^*}$) on uncovered transition metal surfaces [$Q_{S^*} = -\Delta H_s$, where ΔH_s is the heat of reaction $S + * \rightarrow S^*$, $S = \text{CH}_3\text{COO}$ or CH_3COOH]. The DFT calculated heats of CH_3COO^* ($Q_{\text{CH}_3\text{COO}^*}$) and CH_3COOH^* adsorption ($Q_{\text{CH}_3\text{COOH}^*}$) on transition metal surfaces at low coverages (1/9 monolayer) are 302 kJ mol^{-1} vs. 47 kJ mol^{-1} on Ru(0001), 262 kJ mol^{-1} vs. -12 kJ mol^{-1} on Rh(111), 215 kJ mol^{-1} vs. -1 kJ mol^{-1} on Pd(111), 251 kJ mol^{-1} vs. -11 kJ mol^{-1} on Ir(111), and 261 kJ mol^{-1} vs. -5 kJ mol^{-1} on Ni(111) surfaces [18]. The apparent negative heat of CH_3COOH^* adsorption indicates thermodynamically unfavorable adsorption.

Because the heat of adsorption of propionic acid (63 kJ mol^{-1} on Ru(0001) [32]) has approximately the same magnitude with that of acetic acid (47 kJ mol^{-1} on Ru(0001) surfaces [16]), and the heat of adsorption of propionate (344 kJ mol^{-1} on Ru(0001) [32]) has a similar magnitude with that of acetate (302 kJ mol^{-1} on Ru(0001) surfaces [18]), the equilibrium constants $K_{\text{CH}_3\text{COOH}}$ and $K_{\text{CH}_3\text{COO}}$ (Steps 1 and 2 of Scheme 2) can be estimated from the equilibrium constant ($K_{\text{CH}_3\text{CH}_2\text{COOH}}$) for propionic acid adsorption and for propionic acid dissociation ($K_{\text{CH}_3\text{CH}_2\text{COO}}$) on Ru(0001) surfaces of 2.11×10^{-4} and 1.56×10^{10} at 473 K, respectively, based on energetics derived from DFT, the Eyring equation, and partition functions [32]. These estimated equilibrium constants, together with the concentration of CH_3COOH (0.83 M CH_3COOH) and H_2 (50 bar in the gas phase, which corresponds to <0.005 M in the aqueous phase at 473 K [43]), lead to the coverage ratio for CH_3COOH^* -to- $*$ [$\theta_{\text{CH}_3\text{COOH}^*}(\theta_*)^{-1}$] of $\sim 1.75 \times 10^{-4}$ and the coverage ratio for CH_3COO^* -to- $*$ [$\theta_{\text{CH}_3\text{COO}^*}(\theta_*)^{-1}$] larger than 1.76×10^4 . These values translate to negligible CH_3COOH^* coverages and a much larger CH_3COO^* than $*$ coverages during steady-state reactions for the rate data in Figs. 2 and 3. The coverage ratio for CH_3COO^* -to- OH^* [$\theta_{\text{CH}_3\text{COO}^*}(\theta_{\text{OH}^*})^{-1}$] is given by equilibrium constants $K_{\text{CH}_3\text{COOH}}$, $K_{\text{CH}_3\text{COO}}$, $K_{\text{H}_2\text{O}}$, and K_{OH} , as well as H_2O and CH_3COOH concentrations. As an example, the coverage ratio for CH_3COO^* -to- OH^* [$\theta_{\text{CH}_3\text{COO}^*}(\theta_{\text{OH}^*})^{-1}$] at 3.33 M CH_3COOH is estimated to be ~ 0.33 , based on equilibrium constant values either directly reported in

the literature ($K_{\text{H}_2\text{O}}$ and K_{OH} [32]) or approximated from the equilibrium constants for propionic acid adsorption and dissociation ($K_{\text{CH}_3\text{CH}_2\text{COOH}}$, $K_{\text{CH}_3\text{CH}_2\text{COO}}$ [32]) at 473 K. The CH_3COO^* -to- OH^* coverage ratios suggest that CH_3COO^* coverages are similar to OH^* coverages, especially at high CH_3COOH concentrations.

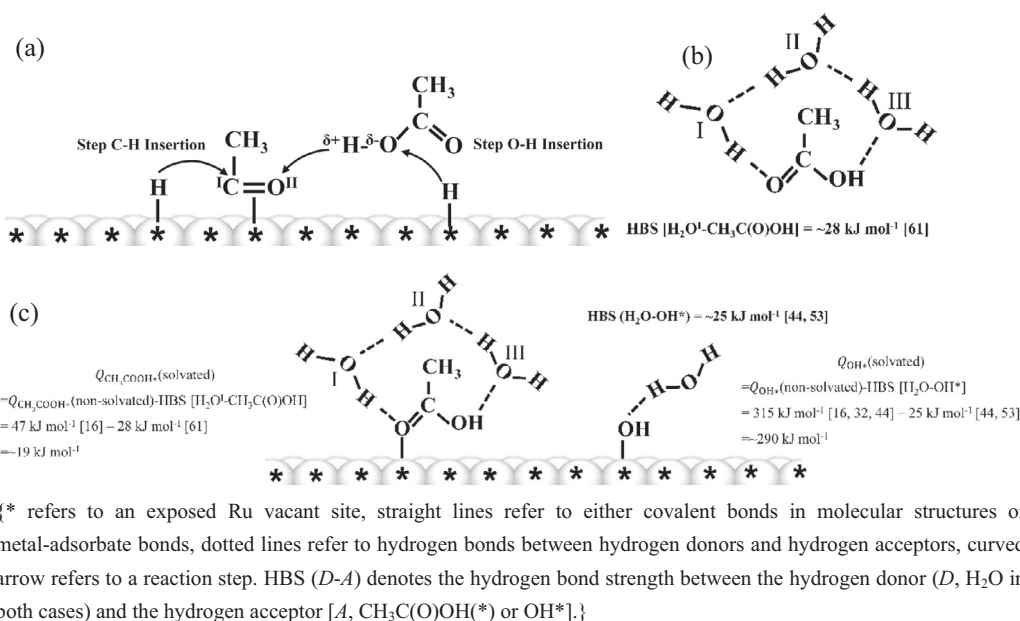
These findings from surface science and density functional theory studies led us to propose that Ru cluster surfaces are preferentially covered with OH^* and, to a smaller extent, CH_3COO^* with their relative abundance given by the H_2O -to- CH_3COOH molar ratio. This assumption leads to much smaller denominator terms associated with $*$, H^* , CH_3COOH^* , and H_2O^* in Eq. (7) than those of OH^* and CH_3COO^* . Thus, the overall acetic acid turnover rate (Eq. (7)) is simplified to

$$r_{\text{overall}} = \frac{[\text{CH}_3\text{COOH}][\text{H}_2]}{(A[\text{CH}_3\text{COOH}] + B[\text{H}_2\text{O}])^2} \quad (9a)$$

$$\text{where } A = \frac{\sqrt{K_{\text{CH}_3\text{COOH}}K_{\text{CH}_3\text{COO}}}}{\sqrt{k_{\text{C-OH}}K_{\text{H}_2}}} \text{ and } B = \frac{K_{\text{H}_2\text{O}}K_{\text{OH}}}{\sqrt{k_{\text{C-OH}}K_{\text{CH}_3\text{COOH}}K_{\text{H}_2}}} \quad (9b)$$

The rate constant $k_{\text{C-OH}}$ and equilibrium constants $K_{\text{CH}_3\text{COOH}}$, $K_{\text{CH}_3\text{COO}}$, K_{H_2} , $K_{\text{H}_2\text{O}}$, and K_{OH} are defined in Scheme 2. This expression is consistent with the observed first order dependency in both CH_3COOH and H_2 at low acetic acid concentrations (<0.83 M; Fig. 2, Section 3.3). An increase in acetic acid concentration to above 0.83 M does not alter the H_2 dependence but decrease the CH_3COOH dependence ($\alpha_{\text{overall}} < 1.0$), as the coverages of inactive surface acetate species relative to OH^* increase and the vacant Ru sites available for assisting with the $\text{CH}_3\text{C}(\text{O})-\text{OH}$ activation concomitantly decrease.

Next, we propose the mechanistic fate of surface acetyl (CH_3CO^*) as they are formed from the kinetically-relevant $\text{CH}_3\text{C}(\text{O})-\text{OH}$ activation step (Step C–OH Cleavage, Scheme 2), because it dictates the selectivity ratio for **Route 1** and **Route 2** (Scheme 1). The rates for **Route 1** ($r_{\text{Route},1}$) refer to the sum of H-insertion rates via the two parallel pathways of: (i) insertion of a chemisorbed H adatom (H^*) into the surface bound carbon (labeled Cⁱ) of $\text{CH}_3\text{C}^i\text{O}^*$ and led to the formation of $\text{CH}_3\text{C}^i\text{HO}^*$ (Step C–H Insertion, Scheme 2), as depicted in Scheme 3a (Step C–H Insertion) and (ii) a proton transfer step involving $\text{CH}_3\text{COO}^{\delta-}-\text{H}^{\delta+}$, $\text{CH}_3\text{CO}^{\text{II}*}$, and H^* , in which $\text{CH}_3\text{COO}^{\delta-}-\text{H}^{\delta+}$ serve as a proton transfer catalyst that transfers its partially charged proton ($\text{H}^{\delta+}$) into the oxygen atom (labeled O^{II}) of acetyl ($\text{CH}_3\text{CO}^{\text{II}*}$) and then regenerate itself by recombining with a chemisorbed H adatom (H^*) (Step O–H Insertion, Scheme 2), as also presented in Scheme 3a (Step O–H Insertion). Following these H-insertion steps, both $\text{CH}_3\text{C}^i\text{HO}^*$ and $\text{CH}_3\text{CO}^{\text{II}*}$ undergo a series of rapid H-insertion steps (Steps 6–10, Scheme 2) and eventually evolve as $\text{CH}_3\text{CH}_2\text{OH}$ (Pathway 1, Scheme 1) and other C_2 derivatives [e.g., ethyl acetate via esterification reaction in Pathway 2 and ethane via secondary oxygen cleavage in Pathway 3 through a surface intermediate $\text{CH}_3\text{CH}_x\text{OH}_y$ ($x = 1$ or 2 , $y = 0$ or 1 , as appeared in Steps 6–8, Scheme 2)]. These H-insertion steps (Step C–H Insertion, Step O–H Insertion, and Steps 6–10) are considered irreversible and kinetically-irrelevant at low acetic acid concentrations [$\{P\}/([\text{CH}_3\text{COOH}])^{-1} < 0.1$, where $\{P\}$ denotes the concentration of product P , $P = \text{CH}_4$, $\text{CH}_3\text{CH}_2\text{OH}$, C_2H_6 , or $\text{CH}_3\text{COOCH}_2\text{CH}_3$] and, at the high H_2 pressures (10–60 bar), to insignificant H-abstraction reactions (reversed Step C–H Insertion, Step O–H Insertion, and Steps 6–10). The sequential reaction between ethanol and hydrogen, which likely occurs via ethoxy intermediates (reversed Step 9, Scheme 2), as proposed from DFT studies [16,47], is negligible, because this is a part of the reverse step of CH_3CHO hydrogenation, the latter has shown to occur at much higher rates (Table 3, $r_{\text{reversed Step 9}} < r_{\text{forward Step 9}}$, Entry 3 vs. Entry 5).



Scheme 3. (a–c) Schematic representations of (a) H-insertions via C–H Insertion and O–H Insertion (Step C–H Insertion and Step O–H Insertion, Scheme 2), (b) optimized solvation shell structure of $\text{H}_2\text{O}-\text{CH}_3\text{COOH}$ complex and hydrogen bond strength of $\text{H}_2\text{O}^{\text{I}}$ -to- $\text{CH}_3\text{C}(\text{O})\text{OH}$ in the absence of metal functions (drawings and energetics adapted from literature [61]), and (c) solvation effects on the heat of acetic acid adsorption ($Q_{\text{CH}_3\text{COOH}^*}$) and heat of hydroxyl adsorption (Q_{OH^*}) in the aqueous phase on Ru surfaces considering the H_2O -adsorbate interactions.

H adatom insertions, either into the C^{I} or O^{II} of $\text{CH}_3\text{C}^{\text{I}}\text{O}^{\text{II}*}$ (Steps C–H Insertion and O–H Insertion, respectively), have been probed with DFT calculations on Ru(0001) surfaces [16,18]. In the gas phase, the direct addition of chemisorbed H^* to the O^{II} in $\text{CH}_3\text{C}^{\text{I}}\text{O}^{\text{II}*}$, which forms $\text{CH}_3\text{C}^{\text{I}}\text{O}^{\text{II}}\text{H}^*$, is energetically unfavorable and thus kinetically insignificant when comparing with the addition of H^* to the carbonyl carbon (C^{I}), which forms $\text{CH}_3\text{C}^{\text{I}}\text{H}\text{O}^{\text{II}*}$ ($E_a = 120 \text{ kJ mol}^{-1}$ for $\text{CH}_3\text{C}^{\text{I}}\text{O}^{\text{II}}\text{H}^*$ formation vs. 79 kJ mol^{-1} for $\text{CH}_3\text{C}^{\text{I}}\text{H}\text{O}^{\text{II}*}$ formation on Ru(0001) surfaces, based on DFT calculations [16,18]). The energetically unfavorable step that forms $\text{CH}_3\text{C}^{\text{I}}\text{O}^{\text{II}}\text{H}^*$ (Step O–H Insertion) may become kinetically significant in the aqueous phase, as proton transport across the water solvent matrix prevails and intensifies in the presence of CH_3COOH as the proton donor via a mechanism similar to those reported for CO– H_2 reactions in the presence of H_2O on Ru/SiO₂ (463 K, 29 bar, $\text{H}_2/\text{CO} = 4.5$, 7 nm mean Ru cluster diameter [48]). For the case of CO– H_2 reactions, H_2O solvates a chemisorbed hydrogen adatom to form a partially charged surface proton ($\text{H}^{\delta+}$) and promotes its insertion into a vicinal CO^* intermediate. Water solvation lowers the activation enthalpy for surface proton transfer, making the hydrogen insertion into the oxygen of CO^* a much more energetically favorable route ($E_a = 75 \text{ kJ mol}^{-1}$) than the hydrogen insertion into the carbon of CO^* either with or without H_2O coordination ($E_a = 91 \text{ kJ mol}^{-1}$ or $E_a = 93 \text{ kJ mol}^{-1}$, respectively) [48–50]. The proton transfer step is expected to be promoted in carboxylic acid solution, because carboxylic acids are more effective proton donors than H_2O ($\text{p}K_a = 4.75$ [51] for acetic acids vs. $\text{p}K_a \sim 15$ for H_2O [52]). First principle calculations considering the solvent environment capture the solvation effects of water in CH_3COOH deprotonation: CH_3COOH dissociates in the aqueous phase (without metal catalysts) through a heterolytic $\text{CH}_3\text{COOH}^{\delta-}-\text{H}^{\delta+}$ cleavage path and forms CH_3COO^- and H^+ that is 1446 kJ mol^{-1} more exothermic than its deprotonation in the gas phase [53]. The H^+ formed in the aqueous environment is solvated by H_2O molecules as a Zundel proton complex [54] (H_5O_2^+ complex) with the H^+ delocalized within the solvent matrix [53]. These experimental observations [48–50,52] and theoretical constructs [53,54] indicate that proton transfer may occur in the presence of $\text{CH}_3\text{COO}^{\delta-}-\text{H}^{\delta+}$,

as it acts as a proton-shuffling catalyst that transports its partially charged hydrogen ($\text{H}^{\delta+}$) to the oxygen atom (O^{II}) of acetyl ($\text{CH}_3\text{CO}^{\text{II}*}$) and regenerates itself by recombining with a chemisorbed hydrogen atom (H^*).

Turnover rates for **Route 2** ($r_{\text{Route},2}$) refer to C–C bond cleavage of CH_3CO^* (Step C–C Cleavage) that forms adsorbed methyl (CH_3^*) and CO^* , followed by sequential hydrogen insertions into these species and their eventual desorption as CH_4 (Steps 11–16, Scheme 2). Similar mechanism has been proposed from diffuse reflectance infrared Fourier transform spectroscopic studies on Ru/ZrO₂ pre-adsorbed with CH_3COOH [15]. The $\nu(\text{C}=\text{O})$ absorption band of adsorbed $\text{CH}_3\text{CH}_2\text{CO}^*$ species at 1621 cm^{-1} diminishes and the bands of CO vibration (1945 cm^{-1} for bridge-bonded CO^* and 2038 cm^{-1} for linearly bonded CO^*) appeared, followed by the $\nu(\text{C}-\text{H})$ of gas phase methane at 3017 cm^{-1} , as the reaction temperature increased from 453 K to 503 K in H_2 . The involvement of these bands suggests the cleavage of $\text{CH}_3\text{CH}_2-\text{CO}^*$ bond leading to the formation of CO, which further hydrogenates and evolves CH_4 [15]. The C–C bond cleavage of CH_3CO^* has also been proposed from DFT studies as the energetically favorable route for methane formation ($E_a = 71 \text{ kJ mol}^{-1}$), as opposed to C–C bond cleavage after sequential H-insertions onto the CH_3CO^* (C–C cleavage barrier, $E_a = 124 \text{ kJ mol}^{-1}$, 108 kJ mol^{-1} , 156 kJ mol^{-1} , and 197 kJ mol^{-1} for CH_3CHO^* , CH_3COH^* , CH_3CHOH^* , and $\text{CH}_3\text{CH}_2\text{O}^*$, respectively), on uncovered Ru(0001) [16,18].

Turnover rates for **Route 1** ($r_{\text{Route},1}$) and **Route 2** ($r_{\text{Route},2}$), measured at low conversions and high H_2 partial pressures (10–60 bar), which lead to low product concentrations $\{[P]/([\text{CH}_3\text{COOH}])^{-1} < 0.1$, where $[P]$ denotes the concentration of product P , $P = \text{CH}_4$, $\text{CH}_3\text{CH}_2\text{-OH}$, C_2H_6 , or $\text{CH}_3\text{COOCH}_2\text{CH}_3$ and negligible H-abstraction rates (reversed steps of Step C–H Insertion, Step O–H Insertion, and Steps 6–10), are derived by applying pseudo steady-state treatments on all reactive intermediates in Scheme 2 (see Supplementary Information, Section S2 for derivation):

$$r_{\text{Route},1} = r_{\text{overall}} \frac{C\sqrt{[\text{H}_2]} + D[\text{CH}_3\text{COOH}]\sqrt{[\text{H}_2]}}{C\sqrt{[\text{H}_2]} + D[\text{CH}_3\text{COOH}]\sqrt{[\text{H}_2]} + 1} \quad (10a)$$

$$r_{\text{Route},2} = r_{\text{overall}} \frac{1}{C\sqrt{[\text{H}_2]} + D[\text{CH}_3\text{COOH}]\sqrt{[\text{H}_2]} + 1} \quad (10b)$$

$$C = \frac{k_{\text{C-H}}\sqrt{K_{\text{H}_2}}}{k_{\text{C-C}}}, \quad D = \frac{k_{\text{O-H}}\sqrt{K_{\text{H}_2}}}{k_{\text{C-C}}} \quad (10c)$$

where r_{overall} is given by Eq. (9a), and the rate constants $k_{\text{C-H}}$, $k_{\text{O-H}}$, and $k_{\text{C-C}}$ and equilibrium constant K_{H_2} are defined in Scheme 2. These rate equations predict a reaction order with respect to H_2 that is unity for the overall rates ($\beta_{\text{overall,predicted}} = 1$, $\beta_{\text{overall,predicted}}$ refers to the predicted H_2 order for r_{overall} , Eqs. (4) and (9a)), greater than or equal to unity for the rates via Route 1 ($\beta_{1,\text{predicted}} = 1-1.5$, $\beta_{1,\text{predicted}}$ denotes the predicted H_2 order for $r_{\text{Route},1}$, Eqs. (9a) and (10a)), and smaller than or equal to unity for the rates via Route 2 ($\beta_{2,\text{predicted}} = 0.5-1$, $\beta_{2,\text{predicted}}$ refers to the predicted H_2 order for $r_{\text{Route},2}$, Eqs. (9a) and (10b)). These predicted reaction orders obtained from Eqs. (9a), (10a), and (10b) are consistent with the measured values ($\beta_{\text{overall}} = 1.1 \pm 0.2$, $\beta_1 = 1.3 \pm 0.1$, and $\beta_2 = 0.6 \pm 0.2$) derived from non-linear regressions of the rate data in Figs. 2 and 3.

The selectivity value (γ , Eq. (6)) becomes, after substituting Eqs. (10a) and (10b) into Eq. (6):

$$\gamma = \frac{r_{\text{Route},1}}{r_{\text{Route},2}} = \frac{k_{\text{C-H}}\sqrt{K_{\text{H}_2}}[\text{H}_2] + k_{\text{O-H}}\sqrt{K_{\text{H}_2}}[\text{H}_2][\text{CH}_3\text{COOH}]}{k_{\text{C-C}}} = C\sqrt{[\text{H}_2]} + D[\text{CH}_3\text{COOH}]\sqrt{[\text{H}_2]} \quad (11)$$

where Parameters C and D are defined in Eq. (10c). Eq. (11) predicts a linear dependence of the selectivity value γ on $[\text{CH}_3\text{COOH}]$ (at constant H_2 partial pressure) and $\sqrt{[\text{H}_2]}$ (at constant $[\text{CH}_3\text{COOH}]$), irrespective of the surface OH^* and CH_3COO^* coverages. These linear dependencies of γ on $[\text{CH}_3\text{COOH}]$ and $\sqrt{[\text{H}_2]}$ are shown in Figs. 4a and 4b, respectively, over the entire operating range of CH_3COOH concentration and H_2 pressure.

The values of the aggregated kinetic and thermodynamic Parameters A , B , C , and D , defined in Eqs. (9b) and (10c), are determined by non-linear regressions of all rate and selectivity data in Figs. 2 and 3, by applying the functional form of Eqs. (9a) and (10a) as the objective functions. The predicted values are included in Figs. 2 and 3 in the form of dotted lines and the parity plots between the predicted and measured rate values are shown in Fig. 5. The optimized parameters are summarized in Table 4, where Parameters A and B both have a standard deviation of less than 10%. The relative magnitudes of A and B (Eq. (9b)) reflect the

relative coverages of CH_3COO^* and OH^* . The low standard deviations of these two Parameters (<10%, Table 4) and their high sensitivity to local perturbations (e.g., a $\pm 20\%$ variation of A or B would cause the sum of the squares of residuals to vary by at least 200%, see perturbation analysis in Fig. S1 in Section S3 of Supplementary Information) allow the use of their values directly together with the CH_3COOH concentration and H_2 pressure to determine the relative abundance of CH_3COO^* ($\theta_{\text{CH}_3\text{COO}^*}$) and OH^* (θ_{OH^*}) on Ru cluster surfaces

$$\theta_{\text{CH}_3\text{COO}^*} = \frac{A[\text{CH}_3\text{COOH}]}{A[\text{CH}_3\text{COOH}] + B[\text{H}_2\text{O}]} \quad (12)$$

$$\theta_{\text{OH}^*} = \frac{B[\text{H}_2\text{O}]}{A[\text{CH}_3\text{COOH}] + B[\text{H}_2\text{O}]} \quad (13)$$

where Parameters A and B are defined in Eq. (9b). Substituting the rate Parameters A and B from Table 4 into these equations gives the fractional coverages of CH_3COO^* and OH^* in the range of 0.05–0.20 and 0.95–0.80, respectively, at 0.17–0.83 M CH_3COOH (aq).

Parameters C and D together with $[\text{CH}_3\text{COOH}]$ reflect the relative rate contributions of H-insertions into the C^{I} of $\text{CH}_3\text{C}^{\text{I}}\text{O}^*$ ($r_{\text{C-H insertion}}$, Step C–H Insertion, Scheme 2) over those into the O^{II} of $\text{CH}_3\text{C}^{\text{O}}\text{O}^*$ ($r_{\text{O-H insertion}}$, Step O–H Insertion, Scheme 2) via the relation of

$$\frac{r_{\text{C-H insertion}}}{r_{\text{O-H insertion}}} = \frac{C}{D[\text{CH}_3\text{COOH}]} \quad (14)$$

where Parameters C and D are defined in Eq. (10c). At concentrated acetic acid solution (≥ 1.67 M), the proposed kinetic model predicts much smaller H-insertion events via C–H Insertion (Step C–H Insertion, Scheme 2) than those via O–H Insertion (Step O–H Insertion, Scheme 2), even at H_2 partial pressures as high as 60 bar [$r_{\text{C-H insertion}}(r_{\text{O-H insertion}})^{-1} = 0.21$, Table 4, 1.67 M CH_3COOH]. The kinetic insignificance of Step C–H Insertion causes the much higher standard deviation (42% of Parameter C vs. 12% of Parameter D , Table 4) and lower sensitivities in response to local perturbation for Parameters C than D (e.g., a $\pm 20\%$ variation in C would vary the sum of the squares of residuals by less than 5% whereas in D would vary by 33%, see perturbation analysis in Fig. S1, Section S3 of Supplementary Information).

In the next section, we discuss the effects of temperature on the $\text{CH}_3\text{C}(\text{O})\text{—OH}^*$ (Step C–OH Cleavage, Scheme 2) rates and

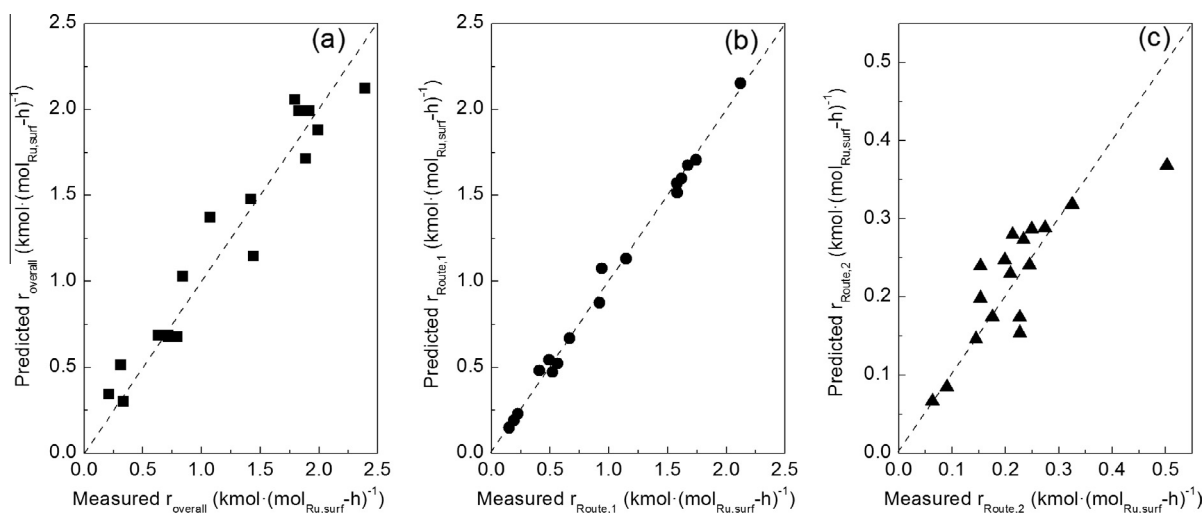


Fig. 5. (a–c) Parity plots for the (a) overall CH_3COOH turnover rates (\blacksquare , r_{overall}), (b) CH_3COOH turnover rates via Route 1 (\bullet , $r_{\text{Route},1}$), and (c) CH_3COOH turnover rates via Route 2 (\blacktriangle , $r_{\text{Route},2}$) at 473 K (0.00–3.33 M CH_3COOH , 10–60 bar H_2 , 100 cm^3 CH_3COOH aqueous solution, 75 mg 4 wt.% Ru/C, 13 nm mean Ru cluster diameter).

Table 4
Rate parameters determined from non-linear regressions of rate data (in Figs. 2 and 3) for aqueous phase hydrogenation of CH₃COOH on dispersed Ru clusters at 473 K^a with the proposed rate equations (Eqs. (9a) and (10a)).

	$A \times 10^{-2} \left(\frac{\text{mol}_{\text{Ru,surf}} \cdot \text{h} \cdot \text{bar} \cdot \text{L}}{\text{mol}^2} \right)^{0.5}$	$B \times 10^{-3} \left(\frac{\text{mol}_{\text{Ru,surf}} \cdot \text{h} \cdot \text{bar} \cdot \text{L}}{\text{mol}^2} \right)^{0.5}$	$C \times 10^{-1} \left(\frac{1}{\text{bar}} \right)^{0.5}$	$D \times 10^{-1} \left(\frac{1}{\text{mol} \cdot \text{bar}^{0.5}} \right)$	$\theta_{\text{CH}_3\text{COO}^*}^b$	$\theta_{\text{OH}^*}^b$	$\frac{r_{\text{C-H insertion}}}{r_{\text{O-H insertion}}}^c$
Value	4.5 ± 0.4	2.9 ± 0.2	1.2 ± 0.5	3.4 ± 0.4	0.20	0.80	0.21

^a 100 cm³ 0.00–3.33 M CH₃COOH (aq), 10–60 bar H₂, 4 wt.% Ru/C (13 nm mean Ru cluster diameter).

^b Coverages estimated from Eq. (9a) with 100 cm³ 0.83 M CH₃COOH (aq) and 50 bar H₂.

^c Rate ratio estimated from Eq. (10a) with 100 cm³ 1.67 M CH₃COOH (aq) and 60 bar H₂.

selectivity values (γ , Eq. (6)) on Ru cluster surfaces predominantly covered with OH* species (>0.8 coverage), attained at low CH₃COOH concentrations (0.83 M) in the aqueous phase; we derive the observed experimental barriers and pre-exponential factors, and lastly, interpret the barriers with Born–Haber thermochemical constructions.

3.5. Effects of temperature on rates, selectivities, and the observed barriers for C–OH cleavage, H-insertion, and C–C cleavage during acetic acid and hydrogen reactions on Ru clusters

CH₃COOH turnover rates (r_{overall}) and instantaneous selectivities (γ , Eq. (6)) are plotted in Fig. 6a and CH₃COOH turnover rates via Route 1 ($r_{\text{Route,1}}$) and Route 2 ($r_{\text{Route,2}}$) in Fig. 6b, both against the inverse temperatures (as 1000 K/T) in the Arrhenius form for reactions in 0.83 M CH₃COOH (aq) and 50 bar H₂ between 423 K and 523 K. Such conditions lead to Ru cluster surfaces predominantly occupied with OH* ($\theta_{\text{OH}^*} > 0.80$, Table 4) and cause the rate of CH₃C(O)–OH scission to increase proportionally with CH₃COOH concentration, because the denominator term associated with the CH₃COO* coverages in Eq. (9a) becomes insignificant relative to that of the OH*. The overall acetic acid turnover rates (Eq. (4)), under these limiting conditions, are simplified to

$$r_{\text{overall}} = k_{\text{eff,overall}} \frac{[\text{CH}_3\text{COOH}][\text{H}_2]}{[\text{H}_2\text{O}]^2} = \frac{1}{B^2} \frac{[\text{CH}_3\text{COOH}][\text{H}_2]}{[\text{H}_2\text{O}]^2} \quad (15)$$

The effective rate constant ($k_{\text{eff,overall}}$, defined in Eq. (4)) equals B^{-2} , where Parameter B is defined in Eq. (9b), which contains rate and equilibrium constants ($k_{\text{C–OH}}$, $K_{\text{CH}_3\text{COOH}}$, K_{H_2} , $K_{\text{H}_2\text{O}}$, and K_{OH}). Decomposing the individual rate constant $k_{\text{C–OH}}$ with the Arrhenius dependence and equilibrium constants $K_{\text{CH}_3\text{COOH}}$, K_{H_2} , $K_{\text{H}_2\text{O}}$, and

K_{OH} with the van't Hoff equation leads to the equation below, which relates the observed barrier (E_a^{obs}) to the barrier for C–OH cleavage ($E_{\text{a,C–OH}}$, Step C–OH Cleavage) and the heats of reactions for Step i (ΔH_i , $i = 1, 3-5$) and the observed pre-exponential factor (A^{obs}) to the pre-exponential factor for C–OH cleavage ($A_{\text{C–OH}}$) and the entropy changes (ΔS_i) for Step i ($i = 1, 3-5$):

$$\begin{aligned} k_{\text{eff,overall}} &= \frac{k_{\text{C–OH}} K_{\text{CH}_3\text{COOH}} K_{\text{H}_2}}{(K_{\text{H}_2\text{O}} K_{\text{OH}})^2} = A^{\text{obs}} \exp\left(-\frac{E_a^{\text{obs}}}{RT}\right) \\ &= A_{\text{C–OH}} \exp\left(\frac{\Delta S_1 + \Delta S_3 - 2\Delta S_4 - 2\Delta S_5}{R}\right) \\ &\quad \times \exp\left(-\frac{E_{\text{a,C–OH}} + \Delta H_1 + \Delta H_3 - 2\Delta H_4 - 2\Delta H_5}{RT}\right) \end{aligned} \quad (16)$$

$$E_a^{\text{obs}} = E_{\text{a,C–OH}} + \Delta H_1 + \Delta H_3 - 2\Delta H_4 - 2\Delta H_5 \quad (17)$$

$$A^{\text{obs}} = A_{\text{C–OH}} \exp\left(\frac{\Delta S_1 + \Delta S_3 - 2\Delta S_4 - 2\Delta S_5}{R}\right) \quad (18)$$

The observed barrier, derived from regression of rate data in Fig. 6a, is 42 kJ mol⁻¹. These heats of reaction ($\Delta H_1 + \Delta H_3 - 2\Delta H_4 - 2\Delta H_5$) can be further decomposed into the heats of CH₃COOH and OH adsorption at a Ru site [$Q_{S^*} = -\Delta H_s$, where ΔH_s is the heat of reaction for the adsorption of species S ($S + * \rightarrow S^*$), $S = \text{CH}_3\text{COOH}$ or OH] and the bond dissociation energies for H–H (BDE_{H_2}) and H–OH ($BDE_{\text{H}_2\text{O}}$) with a Born–Haber thermochemical cycle construction, as shown in Supplementary Information, Section S4. This treatment leads to a simplified expression for E_a^{obs} :

$$E_a^{\text{obs}} = E_{\text{a,C–OH}} - Q_{\text{CH}_3\text{COOH}^*} + 2Q_{\text{OH}^*} + BDE_{\text{H}_2} - 2BDE_{\text{H}_2\text{O}} \quad (19)$$

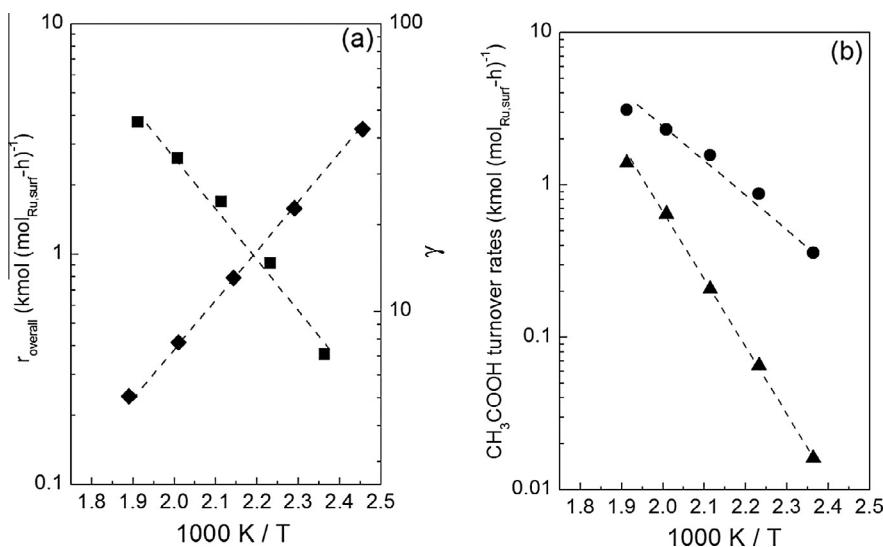


Fig. 6. (a and b) Effects of temperature on (a) overall CH₃COOH turnover rates (■, r_{overall}) and instantaneous selectivity ratio γ (◆, in Eq. (6)) and on (b) CH₃COOH turnover rates via Route 1 (●, $r_{\text{Route,1}}$) and Route 2 (▲, $r_{\text{Route,2}}$) at 423–523 K (100 cm³ of 0.83 M CH₃COOH aqueous solution, 50 bar H₂, 10 mg 4 wt.% Ru/C, 13 nm mean Ru cluster diameter).

where BDE_{H_2} and BDE_{H_2O} are 436 kJ mol^{-1} [55] and 497 kJ mol^{-1} [55], respectively. In the aqueous phase, H_2O molecules solvate the adsorbed species (CH_3COOH^* , OH^*) and the $CH_3C(O)-OH^*$ activation transition state, $[CH_3CO \cdots OH]^\ddagger$ (Step C–OH Cleavage, Scheme 2). The different extents of solvation between the CH_3COOH^* and $[CH_3CO \cdots OH]^\ddagger$ transition state affect the $CH_3C(O)-OH^*$ dissociation barrier ($E_{a,C-OH}$), whereas the solvent–adsorbate interactions between the solvent (H_2O) and CH_3COOH^* (aq) and OH^* (aq) affect their respective heats of adsorption ($Q_{CH_3COOH^*}$ and Q_{OH^*}). These effects of solvation on the $CH_3C(O)-OH^*$ dissociation barrier ($E_{a,C-OH}$) and heats of CH_3COOH and OH adsorption ($Q_{CH_3COOH^*}$ and Q_{OH^*}) alter the observed barrier, E_a^{obs} , through Eq. (19).

The barrier for $RC(O)-OH$ ($R = CH_3$ or CH_3CH_2) dissociation ($E_{a,C-OH}$) on uncovered Ru(0001) surfaces in vacuum is determined to be $\sim 50 \text{ kJ mol}^{-1}$ with DFT (50 kJ mol^{-1} for CH_3COOH [16] and 47 kJ mol^{-1} for CH_3CH_2COOH [32], respectively). In the aqueous phase, the net effects of solvation on the barrier for $CH_3C(O)-OH$ activation depend on the lateness of the $[CH_3CO \cdots OH]^\ddagger$ transition state. The DFT derived heats of reaction for the initial $CH_3C(O)-OH$ bond dissociation on Ru(0001) are mildly exothermic (-25 kJ mol^{-1} for CH_3COOH [16] and -35 kJ mol^{-1} for CH_3CH_2COOH [32]), indicating an early transition state by Hammond–Lefler postulation [56,57]. For an early transition state, the solvation effects on the transition state energetics are likely insignificant, because CH_3COOH^* and $[CH_3CO \cdots OH]^\ddagger$ are solvated to similar extents. Similar conclusions have been drawn for cyclohexene hydrogenation catalyzed by Pt in the organic phase with cyclohexane, *n*-heptane, *p*-dioxane, ethyl acetate, methanol, benzene, or cyclohexene as the solvent, in which H_2 dissociation is the kinetically-relevant step and the transition state complexes $[H \cdots H]^\ddagger$ resemble solvated, intact H_2 molecules [58,59].

CH_3COOH binds to transition metal surfaces {Ru(0001) [16,18,60], Pt(111) [18,26], Pd(111) [18,53]} through both of its oxygen atoms in di- σ configurations. The heat of CH_3COOH^* adsorption in this configuration is 47 kJ mol^{-1} on uncovered Ru(0001) surfaces [16] but in the aqueous phase, it becomes smaller because of solvent–adsorbate interactions, as shown previously from first principle calculations of CH_3COOH adsorption on Pd(111) [53]. The two Pd–O bond distances in the adsorbed $CH_3CO^I-O^IIH^*$ are lengthened when surrounded by H_2O molecules, i.e., from 2.24 \AA to 2.35 \AA for Pd–O^I and from 2.13 \AA to 2.18 \AA for Pd–O^{II} when a CH_3COOH is solvated with eight water molecules in a Pd(111) unit cell comparing to those in the vapor phase, because of the additional stabilization through hydrogen bonds [53]. The extent of solvation is estimated to decrease the heat of CH_3COOH adsorption by $\sim 28 \text{ kJ mol}^{-1}$ compared to that without solvation, derived by assuming the most stable aqueous structure of CH_3COOH solvated by three vicinal H_2O molecules and only a hydrogen from one of the three H_2O molecules interacts directly with the carbonyl oxygen, as can be seen from Schemes 3b and 3c. One water molecule (labeled H_2O^I) forms a hydrogen bond with carbonyl oxygen of CH_3COOH and then interconnects with the other two water molecules (H_2O^{II} and H_2O^{III}) through hydrogen bonds. The third water molecule (H_2O^{III}) forms another hydrogen bond with the proton of CH_3COOH . These water molecules form

a solvation shell around the acetic acid, with the hydrogen bond strength between the carbonyl oxygen to the first water molecule [$H_2O^I-CH_3C(O)OH$] of 28 kJ mol^{-1} (Scheme 3b), as shown previously from *ab initio* molecular dynamic calculations in the absence of metal surfaces [61]. The H_2O solvation depicted in Scheme 3c is estimated to result in less exothermic interactions between the CH_3COOH and Ru surfaces with an estimated heat of CH_3COOH^* adsorption ($Q_{CH_3COOH^*}$) of 19 kJ mol^{-1} . Similar effects of H_2O solvation were reported for phenol adsorption on Pt(111) surfaces, on which the heat of phenol adsorption determined from *ab initio* molecular dynamics decreased by 21 kJ mol^{-1} from 172 kJ mol^{-1} in the gas phase (without solvation) to 151 kJ mol^{-1} in the aqueous phase, because of H_2O solvation [9]. Similarly, the heat of phenol adsorption on Ni(111) surfaces was decreased by 11 kJ mol^{-1} , from 96 kJ mol^{-1} to 85 kJ mol^{-1} as a result of H_2O solvation [9].

The heat of hydroxyl adsorption (Q_{OH^*}) on Ru(0001) surfaces is calculated to be $\sim 315 \text{ kJ mol}^{-1}$ with DFT [16,32,44]. The interactions of H_2O solvent and OH^* through hydrogen bonds decrease the extent of metal– OH^* interactions, as inferred from the increase in metal– OH^* bond distance upon water solvation by 0.12 \AA (from 1.97 \AA to 2.09 \AA) on Ru(0001) [44]. Similar extents of solvation are expected for the interactions between H_2O^* and Ru(0001) surfaces, as Ru–O bond in Ru– H_2O^* was elongated by $\sim 0.16 \text{ \AA}$ (from 2.29 \AA to 2.45 \AA) as a result of water solvation [44]. In the aqueous phase, the heat of adsorption of a single H_2O molecule is determined to be around 17 kJ mol^{-1} (mol of adsorbed H_2O)⁻¹ on Ru(0001) surfaces, by subtracting the energies of H_2O^* –solvent (H_2O) interactions from the total heats of bilayer water adsorption, whereas the similar adsorption step in the vacuum (without any lateral interaction) is about 40 kJ mol^{-1} [44]. These energies indicate that solvation decreases the heat of H_2O^* adsorption by 23 kJ mol^{-1} . Similar solvation effects have been shown on Pd(111) surfaces, on which the heat of a single H_2O adsorption is decreased by 27 kJ mol^{-1} when two H_2O molecules are solvating a H_2O^* [53]. The heat of OH^* adsorption (Q_{OH^*}) on Ru clusters in the aqueous phase is therefore estimated to be approximately 290 kJ mol^{-1} , 25 kJ mol^{-1} lower than those without water solvation and hydrogen bonds, by accounting for the hydrogen bond interactions (one hydrogen bond per OH^* , Scheme 3c). Substitutions of these energies ($E_{a,C-OH}$, $Q_{CH_3COOH^*}$, Q_{OH^*} , BDE_{H_2} , and BDE_{H_2O}) with or without considering the solvation effects into Eq. (19) lead to the predicted barriers, E_a^{obs} (predicted, with solvation) and E_a^{obs} (predicted, without solvation), of 53 kJ mol^{-1} and 75 kJ mol^{-1} , respectively, as summarized in Table 5. The predicted barrier by considering the solvation effects [E_a^{obs} (predicted, with solvation) = 53 kJ mol^{-1}] is in agreement with the observed barrier of 42 kJ mol^{-1} (from Fig. 6a) and consistent with the previously measured value of 32 kJ mol^{-1} on Ru/C (on 14 nm Ru cluster diameter [16]). In contrast, the estimated barrier of 75 kJ mol^{-1} without considering the solvation effects on $CH_3C(O)-OH$ dissociation ($E_{a,C-OH}$) and the heats of CH_3COOH and OH adsorption ($Q_{CH_3COOH^*}$ and Q_{OH^*}) deviates largely from the measured values (42 kJ mol^{-1} from this study and 32 kJ mol^{-1} from [16]).

The observed barriers for Route 1 and Route 2 were determined to be $39 \pm 3 \text{ kJ mol}^{-1}$ (for H-insertion) and $79 \pm 4 \text{ kJ mol}^{-1}$

Table 5

DFT calculated energies of the barrier and heat of adsorption terms appeared in Eq. (19) with or without considering H_2O solvation effects, the H–H and H–OH bond dissociation energies, and the predicted barriers derived from these energies.

	$E_{a,C-OH}$ (kJ mol ⁻¹)	$Q_{CH_3COOH^*}$ (kJ mol ⁻¹)	Q_{OH^*} (kJ mol ⁻¹)	BDE_{H_2} (kJ mol ⁻¹)	BDE_{H_2O} (kJ mol ⁻¹)	E_a^{obs} (predicted) ^a (kJ mol ⁻¹)
With H_2O solvation effects	50 [16,32]	19 [16,61]	290 [16,32,44]	436 [55]	497 [55]	53
Without H_2O solvation effects	50 [16,32]	47 [16]	315 [16,32,44]	436 [55]	497 [55]	75

^a Predicted barriers were determined by substituting the energies $E_{a,C-OH}$, $Q_{CH_3COOH^*}$, BDE_{H_2} , and BDE_{H_2O} into Eq. (19).

(for C–C cleavage), respectively, from linear regressions of the rate data in Fig. 6b. The observed barrier for H-insertion is lower than that for C–C cleavage, and thus the instantaneous selectivity decreases with increasing temperature, consistent with the previous findings on Ru/C catalysts [16,18]. Decomposing the γ value in Eq. (11) into entropic and enthalpic terms by expressing the rate constants k_{C-H} , k_{O-H} , and k_{C-C} with their respective Arrhenius dependence and equilibrium constants K_{H_2} and K_{CH_3COOH} with the van't Hoff equation gives

$$\begin{aligned} \gamma = \frac{r_{Route,1}}{r_{Route,2}} = & \frac{A_{C-H}}{A_{C-C}} \exp\left(\frac{\Delta S_3}{2R}\right) \\ & \times \exp\left(-\frac{(E_{a,C-H} - E_{a,C-C} + 0.5\Delta H_3)}{RT}\right) [H_2]^{0.5} \\ & + \frac{A_{O-H}}{A_{C-C}} \exp\left(\frac{\Delta S_3}{2R}\right) \\ & \times \exp\left(-\frac{(E_{a,O-H} - E_{a,C-C} + 0.5\Delta H_3)}{RT}\right) [H_2]^{0.5} [CH_3COOH] \end{aligned} \quad (20)$$

Parameter pairs A_{C-H} and $E_{a,C-H}$, A_{O-H} and $E_{a,O-H}$, and A_{C-C} and $E_{a,C-C}$ are the pre-exponential factors and activation barriers for the elementary steps occurred in parallel after CH_3CO^* formation (Steps C–H Insertion, O–H Insertion, C–C Cleavage, respectively, in Scheme 2). Parameters ΔS_3 is the entropic changes and ΔH_3 the heat of reaction for Step 3 in Scheme 2. The observed decrease in γ with increasing temperature is originated from the lower intrinsic barriers for both the H^* insertion ($E_{a,C-H}$) and $H^{\delta+}$ insertion ($E_{a,O-H}$) steps than for the C–C bond cleavage ($E_{a,C-C}$, Step C–C Cleavage), as well as from the contribution arising from the exothermic adsorptions of H_2 ($0.5\Delta H_3$), as described by Eq. (20). Rates for the two parallel H-insertion steps of CH_3CO^* , which occur via H^* insertion (Step C–H Insertion) or $CH_3COO^{\delta-}-H^{\delta+}$ catalyzed proton transfer (Step O–H Insertion), likely acquire different sensitivities with temperature, but their individual dependencies could not be resolved with the existing rate data, because such a pursuit would require complete sets for intrinsic rate data of Step C–H Insertion and Step O–H Insertion over a range of temperatures followed by detailed kinetic treatments, which is beyond the scope of this paper. The barriers for H^* insertion into either C^I or O^{II} of CH_3CO^{II} ($E_{a,C-H}$ for Step C–H Insertion and $E_{a,O-H}$ for Step O–H Insertion, respectively) were determined from DFT to be 78 kJ mol^{-1} or 120 kJ mol^{-1} on Ru(0001) surfaces [16]. These barriers, computed on bare Ru(0001) surfaces, cannot be directly compared with the measured barriers, because these calculations did not account for the H_2O solvation effects on the stability of reactants and transition states in polar environment and for the possibility of H_2O involvement in assisting with the proton transfer ($H^{\delta+}$ transfer) reactions (Step O–H Insertion, Scheme 2). Water molecules could preferentially stabilize different surface intermediates, vary the heats of surface reactions, and in turn affect activation barriers, as evident for 1,3-cyclohexadienol (enol) to 3-cyclohexenone (keto) tautomerization on Pt(111) and Ni(111) surfaces. Water molecules solvate the product, 3-cyclohexenone (keto), to a larger extent than the reactant, 1,3-cyclohexadienol (enol), and therefore increase the reaction exothermicity-the heat of tautomerization reaction becomes more negative by -77 kJ mol^{-1} on Pt(111) and -103 kJ mol^{-1} on Ni(111). Such increases in reaction exothermicity cause a concomitant decrease in the activation barrier, i.e., by 63 kJ mol^{-1} on Pt(111) and 35 kJ mol^{-1} on Ni(111) from those in the vapor phase [9]. Theoretical simulations taking water solvation effects into account would be required to further interpret the promotional effects of H_2O in the proton-type hydrogen transfer during the initial CH_3CO^* hydrogenation to better discern the relative contributions from the two H-insertion steps and allow a better interpretation on the observed barriers for Route 1 and Route 2.

4. Conclusions

Catalytic pathways for acetic acid and hydrogen reactions on dispersed Ru clusters in the aqueous medium are established from time-dependent product evolution profiles, initial rates, and isotopic exchange distributions, measured with a gradientless batch reactor. $CH_3COOH-H_2$ reactions occur via a kinetically-relevant $CH_3C(O)-OH$ activation step that forms a surface acetyl intermediate, before its sequential reactions via two distinct routes of either H-insertion or C–C bond cleavage to evolve C_2 products (ethanol, ethane, and their derivative, ethyl acetate) or C_1 (methane) products, respectively, on Ru cluster surfaces nearly saturated with hydroxyl (OH^*) and acetate (CH_3COO^*) species. Acetic acid conversion rates increase linearly with H_2 pressure but exhibit diverse dependencies on CH_3COOH concentration (from first to nearly zero order), because CH_3COOH generates inactive surface acetates that titrate the OH^* and $*$ from Ru sites, thus reducing the Ru vacant sites required for the $CH_3C(O)-OH$ activation.

Surface acetyl ($CH_3C^I O^{II*}$) accepts either a H^* atom into its C^I before successive hydrogenation or a partially charged hydrogen ($H^{\delta+}$) derived from $CH_3COO^{\delta-}-H^{\delta+}$ as a proton transfer catalyst into its O^{II} to form ethanol and its derivatives (ethane and ethyl acetate). Alternatively, it may cleave its C–C bond on an adjacent, unoccupied metal site ($*$), followed by sequential successive hydrogenation, and eventually evolve two CH_4 molecules. The selectivities toward ethanol and its derivatives, which reflect the relative rates of H-insertion versus C–C bond cleavage steps, are dictated by the H_2 partial pressure and CH_3COOH concentration, because they determine the concentrations of the reactive hydrogen adatoms and protons (as H^* or $H^{\delta+}$) required for the two competitive hydrogenation routes. The observed barrier for $CH_3C(O)-OH$ activation on Ru cluster surfaces mostly occupied with OH^* species was found to be 42 kJ mol^{-1} , in agreement with the value predicted from density functional theory calculations on Ru(0001) single crystal surfaces after considering the effects of H_2O solvation on the adsorbed intermediates and on the $CH_3C(O)-OH$ activation transition state. The rate ratios toward H-insertion versus C–C bond cleavage decrease with increasing temperature, because of the higher barriers for C–C bond cleavage than H-insertions. This study describes the catalytic sojourns and fate of a simple carboxylic acid (acetic acid) during aqueous phase hydrogenation on dispersed Ru clusters and demonstrates the coverage effects and involvement of both the hydrogen adatom and $CH_3COO^{\delta-}-H^{\delta+}$ proton transfer catalyst in hydrogenation reactions that ultimately determine the relative distributions of C_2 -to- C_1 product.

Acknowledgments

We acknowledge supports from the Bioenergy Technologies Office of the U.S. Department of Energy and Natural Sciences and Engineering Research Council of Canada (NSERC). The Pacific Northwest National Laboratory is operated for the Department of Energy by Battelle under contract AC0676RLO1830. Junnan Shangguan acknowledges Hatch Graduate Scholarship for Sustainable Energy Research. The authors would also like to thank Prof. Johannes A. Lercher (Technische Universität München, Pacific Northwest National Laboratory), Sebastian Eckstein, Peter Hintermeier, and Dr. Eszter Baráth (Technische Universität München) for helpful discussions, and Dr. Johnathan E. Holladay (Pacific Northwest National Laboratory) and Ms. Corinne Drennan (Pacific Northwest National Laboratory) facilitated the collaboration.

Appendix A. Supplementary material

Supplementary data associated with this article can be found, in the online version, at <http://dx.doi.org/10.1016/j.jcat.2016.04.024>.

References

- [1] G.W. Huber, S. Iborra, A. Corma, Synthesis of transportation fuels from biomass: chemistry, catalysts, and engineering, *Chem. Rev.* 106 (2006) 4044–4098.
- [2] Q. Zhang, J. Chang, T. Wang, Y. Xu, Review of biomass pyrolysis oil properties and upgrading research, *Energy Convers. Manage.* 48 (2007) 87–92.
- [3] S. Czernik, A.V. Bridgwater, Overview of applications of biomass fast pyrolysis oil, *Energy Fuels* 18 (2004) 590–598.
- [4] D.C. Elliott, Historical developments in hydroprocessing bio-oils, *Energy Fuels* 21 (2007) 1792–1815.
- [5] A.H. Zacher, M.V. Olarte, D.M. Santosa, D.C. Elliott, S.B. Jones, A review and perspective of recent bio-oil hydrotreating research, *Green Chem.* 16 (2014) 491–515.
- [6] C. Zhao, J. He, A.A. Lemonidou, X. Li, J.A. Lercher, Aqueous-phase hydrodeoxygenation of bio-derived phenols to cycloalkanes, *J. Catal.* 280 (2011) 8–16.
- [7] C. Zhao, S. Kasakov, J. He, J.A. Lercher, Comparison of kinetics, activity and stability of Ni/HZSM-5 and Ni/Al₂O₃-HZSM-5 for phenol hydrodeoxygenation, *J. Catal.* 296 (2012) 12–23.
- [8] C. Zhao, J.A. Lercher, Selective hydrodeoxygenation of lignin-derived phenolic monomers and dimers to cycloalkanes on Pd/C and HZSM-5 catalysts, *ChemCatChem* 4 (2012) 64–68.
- [9] Y. Yoon, R. Rousseau, R.S. Weber, D. Mei, J.A. Lercher, First-principles study of phenol hydrogenation on Pt and Ni catalysts in aqueous phase, *J. Am. Chem. Soc.* 136 (2014) 10287–10298.
- [10] Y. Yang, Z. Du, Y. Huang, F. Lu, F. Wang, J. Gao, J. Xu, Conversion of furfural into cyclopentanone over Ni–Cu bimetallic catalysts, *Green Chem.* 15 (2013) 1932–1940.
- [11] Y. Nakagawa, K. Takada, M. Tamura, K. Tomishige, Total hydrogenation of furfural and 5-hydroxymethylfurfural over supported Pd–Ir alloy catalyst, *ACS Catal.* 4 (2014) 2718–2726.
- [12] X.-L. Li, J. Deng, J. Shi, T. Pan, C.-G. Yu, H.-J. Xu, Y. Fu, Selective conversion of furfural to cyclopentanone or cyclopentanol using different preparation methods of Cu–Co catalysts, *Green Chem.* (2015).
- [13] Z. He, X. Wang, Required catalytic properties for alkane production from carboxylic acids: hydrodeoxygenation of acetic acid, *J. Energy Chem.* 22 (2013) 883–894.
- [14] H. Wan, R.V. Chaudhari, B. Subramaniam, Aqueous phase hydrogenation of acetic acid and its promotional effect on p-cresol hydrodeoxygenation, *Energy Fuels* 27 (2013) 487–493.
- [15] L. Chen, Y. Li, X. Zhang, Q. Zhang, T. Wang, L. Ma, Mechanistic insights into the effects of support on the reaction pathway for aqueous-phase hydrogenation of carboxylic acid over the supported Ru catalysts, *Appl. Catal. A: Gen.* 478 (2014) 117–128.
- [16] H. Olcay, Y. Xu, G.W. Huber, Effects of hydrogen and water on the activity and selectivity of acetic acid hydrogenation on ruthenium, *Green Chem.* 16 (2014) 911–924.
- [17] Z. Wang, G. Li, X.L.Y. Huang, A. Wang, W. Chu, X. Wang, N. Li, Aqueous phase hydrogenation of acetic acid to ethanol over Ir–MoO_x/SiO₂ catalyst, *Catal. Commun.* 43 (2014) 38–41.
- [18] H. Olcay, L. Xu, Y. Xu, G.W. Huber, Aqueous-phase hydrogenation of acetic acid over transition metal catalysts, *ChemCatChem* 2 (2010) 1420–1424.
- [19] H. Wan, A. Vitter, R.V. Chaudhari, B. Subramaniam, Kinetic investigations of unusual solvent effects during Ru/C catalyzed hydrogenation of model oxygenates, *J. Catal.* 309 (2014) 174–184.
- [20] J. Lee, Y. Xu, G.W. Huber, High-throughput screening of monometallic catalysts for aqueous-phase hydrogenation of biomass-derived oxygenates, *Appl. Catal. B: Environ.* 140–141 (2013) 98–107.
- [21] J. He, C. Zhao, J.A. Lercher, Impact of solvent for individual steps of phenol hydrodeoxygenation with Pd/C and HZSM-5 as catalysts, *J. Catal.* 309 (2014) 362–375.
- [22] W. Rachmady, M.A. Vannice, Acetic acid hydrogenation over supported platinum catalysts, *J. Catal.* 192 (2000) 322–334.
- [23] W. Rachmady, M.A. Vannice, Acetic acid reduction to acetaldehyde over iron catalysts, *J. Catal.* 208 (2002) 158–169.
- [24] T. Yokoyama, N. Yamagata, Hydrogenation of carboxylic acids to the corresponding aldehydes, *Appl. Catal. A: Gen.* 221 (2001) 227–239.
- [25] R. Pestman, R.M. Koster, J.A.Z. Pieterse, V. Ponc, Reactions of carboxylic acids on oxides: 1. Selective hydrogenation of acetic acid to acetaldehyde, *J. Catal.* 168 (1997) 255–264.
- [26] K.I. Gursahani, R. Alcalá, R.D. Cortright, J.A. Dumesic, Reaction kinetics measurements and analysis of reaction pathways for conversions of acetic acid, ethanol, and ethyl acetate over silica-supported Pt, *Appl. Catal. A: Gen.* 222 (2001) 369–392.
- [27] R. Alcalá, J.W. Shabaker, G.W. Huber, M.A. Sanchez-Castillo, J.A. Dumesic, Experimental and DFT studies of the conversion of ethanol and acetic acid on PtSn-based catalysts, *J. Phys. Chem. B* 109 (2005) 2074–2085.
- [28] X. Shen, L.-J. Garces, Y. Ding, K. Laubernds, R.P. Zenger, M. Aindow, E.J. Neth, S.L. Suib, Behavior of H₂ chemisorption on Ru/TiO₂ surface and its application in evaluation of Ru particle sizes compared with TEM and XRD analyses, *Appl. Catal. A: Gen.* 335 (2008) 187–195.
- [29] V. Pallassana, M. Neurock, Reaction paths in the hydrogenolysis of acetic acid to ethanol over Pd(111), Re(0001), and PdRe alloys, *J. Catal.* 209 (2002) 289–305.
- [30] J. Lu, S. Behtash, A. Heyden, Theoretical investigation of the reaction mechanism of the decarboxylation and decarbonylation of propanoic acid on Pd(111) model surfaces, *J. Phys. Chem.* (2012) 14328–14341.
- [31] J. Lu, S. Behtash, M. Faheem, A. Heyden, Microkinetic modeling of the decarboxylation and decarbonylation of propanoic acid over Pd(111) model surfaces based on parameters obtained from first principles, *J. Catal.* 305 (2013) 56–66.
- [32] J. Lu, M. Faheem, S. Behtash, A. Heyden, Theoretical investigation of the decarboxylation and decarbonylation mechanism of propanoic acid over a Ru(0001) model surface, *J. Catal.* 324 (2015) 14–24.
- [33] G. Bergeret, P. Gallezot, Particle size and dispersion measurements, in: *Handbook of Heterogeneous Catalysis*, Wiley-VCH Verlag GmbH & Co. KGaA, 2008.
- [34] H. Wan, A. Vitter, R.V. Chaudhari, B. Subramaniam, Kinetic investigations of unusual solvent effects during Ru/C catalyzed hydrogenation of model oxygenates, *J. Catal.* 309 (2014) 174–184.
- [35] P.B. Weisz, C.D. Prater, Interpretation of measurements in experimental catalysis, in: V.I.K.W.G. Frankenburg, E.K. Rideal (Eds.), *Advances in Catalysis*, Academic Press, 1954, pp. 143–196.
- [36] C.R. Wilke, P. Chang, Correlation of diffusion coefficients in dilute solutions, *AIChE J.* 1 (1955) 264–270.
- [37] W. Hayduk, H. Laudie, Prediction of diffusion coefficients for nonelectrolytes in dilute aqueous solutions, *AIChE J.* 20 (1974) 611–615.
- [38] J.G. Bleazard, T.F. Sun, A.S. Teja, The thermal conductivity and viscosity of acetic acid–water mixtures, *Int. J. Thermophys.* 17 (1996) 111–125.
- [39] S. Mukherjee, M.A. Vannice, Solvent effects in liquid-phase reactions: I. Activity and selectivity during citral hydrogenation on Pt/SiO₂ and evaluation of mass transfer effects, *J. Catal.* 243 (2006) 108–130.
- [40] K.S. Bankole, Uncatalyzed esterification of biomass-derived carboxylic acids, in: *Chemical Engineering*, University of Iowa, 2011. <<http://ir.uiowa.edu/etd/922>>.
- [41] U.K. Singh, M.A. Vannice, Kinetics of liquid-phase hydrogenation reactions over supported metal catalysts—a review, *Appl. Catal. A: Gen.* 213 (2001) 1–24.
- [42] O.A. Abdelrahman, A. Heyden, J.Q. Bond, Analysis of kinetics and reaction pathways in the aqueous-phase hydrogenation of levulinic acid to form γ -valerolactone over Ru/C, *ACS Catal.* 4 (2014) 1171–1181.
- [43] H.A. Pray, C.E. Schweickert, B.H. Minnich, Solubility of hydrogen, oxygen, nitrogen, and helium in water at elevated temperatures, *Ind. Eng. Chem.* 44 (1952) 1146–1151.
- [44] A. Michaelides, A. Alavi, D.A. King, Different surface chemistries of water on Ru(0001): from monomer adsorption to partially dissociated bilayers, *J. Am. Chem. Soc.* 125 (2003) 2746–2755.
- [45] P.J. Feibelman, Partial dissociation of water on Ru(0001), *Science* 295 (2002) 99–102.
- [46] A.R. Garcia, J.L. da Silva, L.M. Ilharco, Chemical adsorption of acetic acid and deuterated acetic acid on Ru(0001), by RAIRS, *Surf. Sci.* 415 (1998) 183–193.
- [47] C.-c. Chiu, A. Genest, N. Rösch, Decomposition of ethanol over Ru(0001): a DFT study, *Top. Catal.* 56 (2013) 874–884.
- [48] D.D. Hibbitts, B.T. Loveless, M. Neurock, E. Iglesia, Mechanistic role of water on the rate and selectivity of Fischer–Tropsch synthesis on ruthenium catalysts, *Angew. Chem. Int. Ed.* 52 (2013) 12273–12278.
- [49] B.T. Loveless, C. Buda, M. Neurock, E. Iglesia, CO chemisorption and dissociation at high coverages during CO hydrogenation on Ru catalysts, *J. Am. Chem. Soc.* 135 (2013) 6107–6121.
- [50] D. Hibbitts, E. Iglesia, Prevalence of bimolecular routes in the activation of diatomic molecules with strong chemical bonds (O₂, NO, CO, N₂) on catalytic surfaces, *Acc. Chem. Res.* 48 (2015) 1254–1262.
- [51] R.N. Goldberg, N. Kishore, R.M. Lennen, Thermodynamic quantities for the ionization reactions of buffers, *J. Phys. Chem. Ref. Data* 31 (2002) 231–370.
- [52] P. Gilli, L. Pretto, V. Bertolasi, G. Gilli, Predicting hydrogen-bond strengths from acid–base molecular properties. The pK_a slide rule: toward the solution of a long-lasting problem, *Acc. Chem. Res.* 42 (2009) 33–44.
- [53] S.K. Desai, V. Pallassana, M. Neurock, A periodic density functional theory analysis of the effect of water molecules on deprotonation of acetic acid over Pd(111), *J. Phys. Chem. B* 105 (2001) 9171–9182.
- [54] M. Tuckerman, K. Laasonen, M. Sprik, M. Parrinello, Abinitio molecular dynamics simulation of the solvation and transport of hydronium and hydroxyl ions in water, *J. Chem. Phys.* 103 (1995) 150–161.
- [55] S.J. Blanksby, G.B. Ellison, Bond dissociation energies of organic molecules, *Acc. Chem. Res.* 36 (2003) 255–263.
- [56] G.S. Hammond, A correlation of reaction rates, *J. Am. Chem. Soc.* 77 (1955) 334–338.
- [57] T.A. Manz, D.S. Sholl, A dimensionless reaction coordinate for quantifying the lateness of transition states, *J. Comput. Chem.* 31 (2010) 1528–1541.
- [58] R.J. Madon, E. Iglesia, Catalytic reaction rates in thermodynamically non-ideal systems, *J. Mol. Catal. A: Chem.* 163 (2000) 189–204.
- [59] R.J. Madon, J.P. O’Connell, M. Boudart, Catalytic hydrogenation of cyclohexene: Part II. Liquid phase reaction on supported platinum in a gradientless slurry reactor, *AIChE J.* 24 (1978) 904–911.
- [60] A.R. Garcia, J.L.d. Silva, L.M. Ilharco, Chemical adsorption of acetic acid and deuterated acetic acid on Ru(0001), by RAIRS, *Surf. Sci.* 415 (1998) 183–193.
- [61] L. Pu, Y. Sun, Z. Zhang, Hydrogen bonding in hydrates with one acetic acid molecule, *J. Phys. Chem. A* 114 (2010) 10842–10849.